POLITECNICO DI TORINO
Repository ISTITUZIONALE

Active and Selective Ensembles in Oxide-Derived Copper Catalysts for CO2 Reduction

Original
Active and Selective Ensembles in Oxide-Derived Copper Catalysts for CO2 Reduction / Dattila, Federico; Garca-Muelas, Rodrigo; López, Núria. - In: ACS ENERGY LETTERS. - ISSN 2380-8195. - ELETTRONICO. - 5:10(2020), pp. 3176-3184. [10.1021/acsenergylett.0c01777]

Availability:
This version is available at: 11583/2981892 since: 2023-09-11T08:26:35Z

Publisher:
American Chemical Society

Published
DOI:10.1021/acsenergylett.0c01777

Terms of use:

This article is made available under terms and conditions as specified in the corresponding bibliographic description in the repository

Publisher copyright
ACS postprint/Author's Accepted Manuscript

This document is the Accepted Manuscript version of a Published Work that appeared in final form in ACS ENERGY LETTERS, copyright © American Chemical Society after peer review and technical editing by the publisher. To access the final edited and published work see http://dx.doi.org/10.1021/acsenergylett.0c01777.

(Article begins on next page)

12 September 2024

Supporting Information

Active and selective ensembles in oxide-derived copper catalysts for CO_2 reduction

Federico Dattila, Rodrigo García-Muelas, and Núria López*

Institute of Chemical Research of Catalonia (ICIQ), The Barcelona Institute of Science and Technology (BIST), Av. Països Catalans 16. 43007 Tarragona, Spain.

E-mail: nlopez@iciq.es

Contents

List of Figures

List of Tables

S1 Computational Methods

To model the oxide-derived copper (OD-Cu) system, we built slabs of different stoichiometry and allowed them to relax upon Ab initio molecular dynamics (AIMD). Our approximations, such as periodic boundary conditions, density functional, lack of solvent, potential, and electrolyte are severe, but this approach constitutes the first systematic investigation of nanostructuring and formation of new ensembles in OD-Cu.

S1.1 Models

Cu_2O-derived catalysts were modelled as a $2\sqrt{3} \times 2\sqrt{3} - R30°$ Cu_2O supercell (lateral size 21.11Å, thickness 13.69Å, vacuum ∼10Å), presenting 6 Cu_2O layers. To simulate CO_2 reduction conditions, oxygen atoms were removed from the two outermost Cu_2O layers. All the outermost oxygens of the surface Cu_2O layer were taken out. n innermost oxygen atoms were additionally removed to form Rhomboidal (4R), Triangular (4T), and linear (6L) Cu clusters, **Figure 1**. For the triangular system, an additional oxygen atom was removed from the second Cu_2O to mimic pitting. The systems were named nS where n has been defined previously and S is the cluster geometrical shape. Alternatively, oxidized Cu catalysts (oxi-Cu) were obtained by depositing three Cu_2O layers on a commensurate $5\sqrt{3} \times 5\sqrt{3} - R30°$ bulk Cu(111). The surface and subsurface oxygens were removed following the same procedure as for Cu_2O reduction models. To distinguish both classes, red-Cu_2O and oxi-Cu suffixes were appended to the name of each system, such as 4R-red-Cu_2O or 4R-oxi-Cu.

S1.2 Density Functional Theory simulations

Density Functional Theory (DFT) studies were performed with the Vienna Ab Initio Simulation Package (VASP)[1,2] version 5.4.4, using the PBE density functional.[3] Inner electrons were represented by PAW[4] and the monoelectronic states for the valence electrons expanded as plane waves with a kinetic energy cutoff of 450 eV. For Cu, the 11-electrons pseudopotentials (PP) suffice to describe our system, as tests done with the 17-electrons PP indicated that there were not significant differences, **Table S18**. For AIMD and adsorption of intermediates, the Brillouin zone zone was sampled only by the Γ-point: we tested this value against a 2×2, 3×3, 4×4 k-points grid[5] and the differences in energy were lower than 0.01 eV, **Table S19**. We initially tested the Hubbard correction through the Dudarev formalism,[6] using as criterion the formation energy of bulk copper oxide[7–9] and the thermochemical properties and stability of the ensembles. However, experimental values were better described when no Hubbard correction was applied, **Tables S18-S20**, in line with previous work on Cu_xO_y clusters[10,11], so we keep this setup for all the remaining simulations. Additionally, Hubbard correction did not influence the characteristic ensembles, **Figures S20**. During AIMD and intermediate adsorption, the two innermost layers were kept fixed to represent the bulk oxide (metal) for the red-Cu_2O (oxi-Cu) models, whilst the others were free.

S1.3 Ab initio molecular dynamics

We investigated the time evolution of both red-Cu_2O and oxi-Cu models for at least 1 + 10 ps through AIMD (ref 12) at 700 K (canonical ensemble, NVT, Nosé-Hoover thermostat).[13,14] We chose an equilibration time of 1 ps, although all measured properties converged before that threshold. A time step of 3 fs allowed sampling each periodic displacement by at least 16 trajectories, as the maximum calculated Cu-O vibrational frequency was lower than 630 cm^{-1} (period: >50 fs). Further benchmark tests were done for different AIMD temperatures and Hubbard corrections. 4R-red-Cu_2O system underwent AIMD for 1 + 10 ps at 500 K and this benchmark simulation was called 4R-red-Cu_2O-500. Additionally, the final configuration of 4R-red-Cu_2O at 700 K was cooled down at a rate of 0.1 fs K^{-1} to 500 K (2.0 ps ramp + 4.5 ps stabilization) and 300 K (4.0 ps ramp). The resulting simulations were defined 4R-red-Cu_2O-500-R and 4R-red-Cu_2O-300-R. The configuration of the system 4R-oxi-Cu at 5.0 ps of production time was used as input for additional 5.0 ps of AIMD at 700 K and with $U_{\text{eff}} = 6$ eV. Structural characterization of the benchmark systems confirmed that the characteristic surface ensembles did not depend on AIMD temperature and Hubbard correction, **Figures** S18, S19, S20.

S1.4 Reaction intermediates adsorption

Adsorption of relevant reaction intermediates were calculated upon relaxation of red-Cu_2O final AIMD trajectories. We applied the DFT-D2 method to include van der Waals interactions,[15,16] with our C_6 reparametrized coefficients for metals.[17] Implicit solvation was included through the VASPsol code[18,19] as implemented in VASP 5.4.4 while deactivating the dipole correction. The adsorbates were placed only on one side of the slab, thus requiring a dipole correction to remove spurious contributions arising from the asymmetric slab model.[20] Relaxations were converged setting a force threshold of 0.03 eV/Å. All energies are reported using CO_2(g), H_2(g), H_2O(g) and the OD-Cu surfaces as references. The energy of H^+ at 0.0 V vs SHE was derived from H_2 by using the computational hydrogen electrode.[21,22]

S1.5 Hubbard correction

GGA density functionals, such as PBE, may fail to describe the electronic properties of reducible metal oxides due to the self-interaction error.[23] A computationally effective solution is the Dudarev's $U_{\text{eff}} = U - J$ correction.[6] For Cu_2O, an U_{eff} of 6.0-6.5 eV has been proposed in literature, using hybrid functionals (refs 7–9,24) and thermochemistry (ref 25) as references. However, these previous applications of U_{eff} did not provide a good estimation of the band gap.[8,9] As benchmark, we calculated copper oxide formation energy, **Equations S1-S2** as a function of U_{eff} in the spirit of Nie *et al.*[25] G_{H^+} was estimated as $\frac{1}{2}G_{\text{H}_2}$ applying the Computational Hydrogen Electrode.[22]

$$2\text{Cu(s)} + \text{H}_2\text{O(aq)} \longrightarrow \text{Cu}_2\text{O(s)} + 2\text{H}^+ + 2\text{e}^- \tag{S1}$$

$$G_{\mathrm{Cu_2O}} = G_{\mathrm{Cu_2O}} - 2G_{\mathrm{Cu}} - G_{\mathrm{H_2O}} + 2G_{\mathrm{H^+}} - 2|\mathrm{e}^-|U \tag{S2}$$

Table S18 reports the calculated Cu_2O formation energies vs U_{eff}, with $U_{\mathrm{eff}} = U - J$ and $J = 1$ eV. We employed Cu_2O 1×1×1 and Cu 1×1×1 unit cells and we applied Hubbard correction to d Cu electrons for both systems. We corrected theoretical formation energies by solvation and entropy calculated from experimental data,[26] **Equations S3-S4**.

$$\Delta G_{\mathrm{sol}} = G_{\mathrm{H_2O,l}} - G_{\mathrm{H_2O,g}} \tag{S3}$$

$$-T \cdot S = G_{\mathrm{Cu_2O,exp}} - H_{\mathrm{Cu_2O,exp}} \tag{S4}$$

The experimental copper oxide formation energy (ref 26) was best reproduced neglecting any U correction, $G_{\mathrm{Cu_2O}} = 0.96$ vs $G_{\mathrm{Cu_2O,exp}} = 0.94$ eV. Besides, our test showed that the thermochemical properties of the ensembles calculated applying PBE were comparable within $\Delta E < 0.03$ eV ($\Delta E < 0.12$ eV) with the simulations done with PBE+U for $U_{\mathrm{eff}} = 3$ eV ($U_{\mathrm{eff}} = 6$ eV), **Table S20**.

S1.6 Configurational entropy effects on Cu_xO_y stability

O diffusion within Cu layers stabilizes oxides (ref 27) and suboxides by entropy, **Equation S5**. Depending on W, the number of possible configurations, a related configurational entropy S stabilizes the system, with a proportionality constant k_{B} defined as the Boltzmann constant. This formula is valid under the assumption that every configuration has the same probability, $P_n = \frac{1}{W}$. However, a more general formulation accounts for different probabilities of each configuration, P_i, which are functions of their respective energy, degeneracies, and statistical properties of the system,[27–29] **Equation S6**.

$$S = k_{\mathrm{B}} \cdot \ln W \tag{S5}$$

$$S = -k_\mathrm{B} \cdot \sum_{i=1}^{W} P_i \ln P_i \tag{S6}$$

The application of **Equation S6** for all the possible configurations allowed for our systems is far beyond our computational limits. Therefore, we calculated configurational entropy effects assuming equal probability of occurrence among sites, **Equation S5**. We estimated the total number of possible configurations as $N_\text{O-bulk} = \frac{N_\text{Cu}}{2}$, taking as reference the number of oxygen sites in bulk Cu_2O. Given the number of oxygens in the systems after O removal, $N_\text{O-res}$, the number of possible configurations is then expressed by the binomial coefficient, **Equation S7**.

$$W = \binom{N_\text{O-max}}{N_\text{O-res}} = \frac{N_\text{O-max}!}{N_\text{O-res}! \cdot (N_\text{O-max} - N_\text{O-res})!} \tag{S7}$$

The configurational entropy shown in **Table S4** was computed by taking the possible O configurations in the 4-7 outermost layers, within the detection limit of X-ray Photoelectron Spectroscopy ($\approx$ 1-3 nm).[30] Due to the limited lateral size of the $2\sqrt{3} \times 2\sqrt{3}$ cells, we extrapolated their entropy S up to their 100×100 expansion.

S1.7 Pourbaix diagram

We assessed the thermodynamic stability of our models by estimating their Pourbaix diagrams, **Figure S1**. To this end, the final snapshot trajectories of the red-Cu_2O and oxi-Cu systems were compared with Cu/Cu_2O reaction. As reference, two metastable suboxidic phases were also included: Cu_8O and $Cu_{64}O$.[31,32] Both Cu oxidation and Cu_2O reduction were considered, **Equations S8-S9**.

$$2x \cdot \mathrm{Cu} + y \cdot \mathrm{H_2O} \longrightarrow \mathrm{Cu}_{2x}\mathrm{O}_y + 2y \cdot \mathrm{H^+} + 2y \cdot \mathrm{e^-} \tag{S8}$$

$$x \cdot \mathrm{Cu_2O} + 2y \cdot \mathrm{H^+} + 2y \cdot \mathrm{e^-} \longrightarrow \mathrm{Cu}_{2x}\mathrm{O}_{x-y} + y \cdot \mathrm{H_2O} \tag{S9}$$

Table S6 shows the formation energy for all models normalized by the number of e^- transferred. Solvation and configuration entropy at room temperature are reported as well, **Tables S4** and **Table S5**. For comparison, **Table S7** reports the formation energy for the metastable phases Cu_8O and $Cu_{64}O$.[31,32]

Pourbaix diagrams are derived accounting for the equilibrium between two thermodynamic phases.[33] If one phase has a higher thermodynamic formation energy than a competing one, then the latter is expected to be the stable phase at the equilibrium.[34] However, configuration entropy is well-know to play an active role in stabilizing disordered oxides.[27] Therefore, under operating conditions, oxides may be thermodynamically stable due to entropic effects or kinetically trapped since they present borderline-stability.[27,34]

S1.8 X-ray Photoelectron Spectroscopy

The characteristic peaks of X-ray Photoelectron Spectroscopy of Cu 2p and O 1s states were predicted in VASP.[35,36] XPS shift for Cu^0, $Cu^{\delta+}$, Cu^+ (vs crystalline Cu) and O (vs oxidic O) are reported in **Figure S5**.

S1.9 Raman spectra

The predicted Raman spectra shown in **Figure S7** were derived from the AIMD following the procedure reported in ref 37. Only the atoms free to move were considered in the analysis. First, atom velocities were calculated from atomic displacements, $\vec{\Delta r}$, for each AIMD time step, $\Delta t = 3$ fs. Then, velocity autocorrelation function, $\gamma(t_j)$, was calculated as follows: the velocity of each atom for a given time t_j, $\vec{v}_i(t)$, was projected into its velocity in the previous step, $\vec{v}_i(t_{j-1})$. This value was averaged for all N_{atoms} atoms and the result was normalized by dividing against the norm of the previous time step velocity. The values of $\gamma(t_j)$ are therefore a discrete function of each timestep j, **Equations S10-S11**.

$$\vec{v} = \frac{\Delta \vec{r}}{\Delta t} \tag{S10}$$

$$\gamma(t_j) = \frac{\sum_{i}^{N_{\text{atoms}}} \vec{v}_i(t_{j-1}) \cdot \vec{v}_i(t_j)}{\sum_{i}^{N_{\text{atoms}}} \vec{v}_i(t_{j-1}) \cdot \vec{v}_i(t_{j-1})} \tag{S11}$$

The frequency spectrum, shown in **Figure S6**, was then estimated from the discrete Fourier transform of the velocity autocorrelation function following **Equation S12**. N_{steps} is the total number of AIMD steps. Since just the positive frequencies were considered, the absolute values of $P(\omega)$ were plotted vs ω, in cm^{-1}.

$$P(\omega) = \sum_{j=0}^{N_{\text{steps}}-1} \gamma(t_j) e^{-i\omega_j t_j} \tag{S12}$$

$$\omega = \frac{c}{2\Delta t} \tag{S13}$$

S1.10 Surface roughness

Surface roughness was estimated for each step of the AIMD and plotted in **Figure S9**. The process started by ordering all the atoms by their position in z to identify the ones belonging to the surface as those which do not have any other on top. To this end, we applied as criterion that a surface atom cannot have another one at higher height if the angle formed by the vector connecting them and the xy plane (**Figure S8**), φ, is larger than 50 degrees. Therefore, for a surface atom having other atoms on top **Equation S14** must be verified.

$$\tan(\varphi) = \frac{\Delta z}{\sqrt{\Delta x^2 + \Delta y^2}} < 1.15 \tag{S14}$$

Then, applying **Equation S15** to all surface atoms i in each time step j, roughness σ was calculated with respect to the arithmetic average of all heights in that step, $\bar{z}_j$.

$$\sigma_j = \frac{1}{n}\sum_{i=1}^{n} |z_{ij} - \overline{z}_j| \tag{S15}$$

To get an estimation of the enhanced activity of OD-Cu as a consequence of the increase in number of surface sites, **Figure S10**, we defined A_{Cu} as the ratio between surface sites on OD-Cu models (red-Cu_2O and oxi-Cu) and pristine Cu_2O, **Equation S16**.

$$A_{\text{Cu}} = \frac{N_{\text{Cu-surf}}}{N_{\text{Cu-surf}(\text{Cu}_2\text{O})}} \tag{S16}$$

S1.11 Radial distribution function

Radial distribution functions (Cu-Cu and Cu-O) were estimated centering in the atoms belonging to the two outermost Cu_2O layers and assuming a cutoff distance of 7Å with respect to all other atoms. We calculated the distribution of distances, $\eta(r)$, which is the number of atoms at a distance between r and $r + \Delta r$ from a central reference atom and includes all molecular dynamics steps. $\eta(r)$ was then normalized to account for the expected density of atoms corresponding to an annulus (2D), **Equation S17**.

$$g(r)_{2D} = \frac{\eta(r)}{2\pi r \cdot \Delta r \cdot \rho} \tag{S17}$$

For the particular case of the symmetric system (SY-red-Cu_2O), a full volumetric normalization akin to a spherical shell (3D) was applied, **Equation S18**.

$$g(r)_{3D} = \frac{\eta(r)}{4\pi r^2 \cdot \Delta r \cdot \rho} \tag{S18}$$

S1.12 Coordination shell

Two atoms were considered to be coordinated if their distance failed below a certain threshold given by their bond type (Cu-Cu or Cu-O). For Cu-O bonds, the threshold was obtained from the Cu-O radial distribution function, $g_{\text{Cu}-\text{O}}$, **Figure S11**. In bulk Cu_2O, two clear peaks are found at 1.87 and 3.57 Å, while for the AIMD systems, a minimum was found at around 2.5 Å. Therefore, two Cu-O atoms were considered to be bonded if their distance was below that value. For Cu-Cu bonds, the first peak in $g_{\mathrm{Cu-Cu}}$ appears at 2.57 Å and 3.05 Å for Cu (fcc metal) and Cu_2O respectively, **Figure S13c**. During the AIMD, most Cu-Cu bonds lengths fell into these limits. Thus, we assigned a bond value $N_{\text{Cu-Cu}}$ between 0.0 and 1.0 following a decay controlled by the error function (erf), **Equations S19-S20, Figure S13a**.

$$N_{\text{Cu-Cu}} = \left(\frac{1 - \text{erf}(\frac{d_{\text{Cu-Cu}} - 2.7}{0.1})}{2} \right) \tag{S19}$$

$$\text{erf}\,(z) = \frac{2}{\sqrt{\pi}} \cdot \int_0^z \exp(-t^2)dt \tag{S20}$$

S1.13 Bader charges

Bader charges were computed according to standard procedures.[38–41]

S1.14 Ensembles polarization

Ensembles can effectively trap molecules such as CO_2 and OCCO if they are locally polarized. The atoms binding with carbon (either Cu or O), X(C), must be rich in electronic density. Those tethering oxygen, Y(O), are more active when positively polarized. For a CO_2 molecule binding to two Cu atoms through a C and an O, $\eta^2_{\mathrm{C,O}}$, the ensemble polarization can be obtained by adding up the Bader charges of the Cu atoms binding the C and O respectively, $q_{\mathrm{Cu(C)}}$ and $q_{\mathrm{Cu(O)}}$ in **Equation S21**. For the final trajectories of the AIMD, Bader charges ranged from −0.10 to +0.78 $|e^-|$ for Cu and –0.84 to –1.11 $|e^-|$ for O.

$$Q = q_{\mathrm{Cu(C)}} + q_{\mathrm{Cu(O)}} \tag{S21}$$

However, there are many possible deviations from this simple rule. CO_2 can bind through its three constituents $\eta^3_{\mathrm{O,C,O}}$. Some atoms may adsorb on bridge configurations. The central atom may bind to an adsorbed oxygen to form carbonate ($^*CO_3^{2-}$). Also, crucial intermediates to produce C_{2+}, such as oxalate and glyoxylate, bind through more than two constituents. Therefore, the polarization of the active site can be normalized to include all the atoms which bind C and O atoms, $X(\mathrm{C})$ and $Y(\mathrm{O})$ respectively, **Equation S22**.

$$Q = \frac{1}{N_{X(\mathrm{C})}} \left| \sum_{i=1}^{N_{X(\mathrm{C})}} q_{X_i(\mathrm{C})} \right| + \frac{1}{N_{Y(\mathrm{O})}} \left| \sum_{i=1}^{N_{Y(\mathrm{O})}} q_{Y_i(\mathrm{O})} \right| \tag{S22}$$

S2 Supporting Discussion

S2.1 Experimental stabilization of residual oxygen in OD-Cu

The presence of residual oxygen in oxide-derived copper (OD-Cu) catalysts has been strongly debated in literature.[42,43] In general, OD-Cu is a family of catalysts whose composition strongly depends on their history.

Particular synthesis protocols which involve deep oxidation may enable the presence of subsurface or near-surface oxygen.[44–47] 2-4 nm Cu nanoparticles formed during CO_2R conditions are expected to have facile oxygen access on the surface[48] and oxygen depleted phases were characterized for thermally-treated copper[44], pre-reduced Cu_2O nanoparticles[49], and chemically-oxidized Cu nanocubes[50]. O 1s Ambient Pressure XPS (APXPS) found adventitious subsurface oxygens for Cu foil and Cu nanoparticles subjected to several oxidation-reduction cycles[45,51]. X-Ray Photoelectron Spectroscopy (XPS) and X-ray absorption near edge structure (XANES) characterization of $Cu(OH_2)$ nanowires confirmed the high oxygen content under reduction conditions.[46] As indirect proofs, $Cu(OH)_2$-derived catalysts exhibit at -0.56 V vs RHE the typical Raman shift of CuO (390 cm^{-1}) and similar Auger spectra[52]. A 20% fraction of Cu^+ species was still detected on Cu_2O nanocubes catalysts after 2h of electroreduction at -0.95 V vs RHE.[53] Cu_2O fingerprints were confirmed for Auger spectra of Cu(100) under pulsed electrolysis (anodic potential: $+0.6$ V vs RHE, cathodic potential:

-1.0 V vs RHE)[47]. Cu K-edge Extended X-ray Absorption Fine Structure (EXAFS) characterization detected a strong Cu-O path for copper oxychlorides derived catalysts[54]. Cu^+ signals for OD-Cu under operation were detected as well *via* X-ray Absorption Spectroscopy (XAS) (refs 55–58). As further evidences based on product distribution, C_{2+} selectivity increased for high surface polarization[47], specific actives sites[59], and under O_2 and CO_2 co-electrolysis for OD-Cu.[60]

Instead, when OD-Cu is produced from Cu foils oxidized by air or by mild anodic potentials, oxygen atoms are not detectable under reduction conditions within detection limits.[61–63] Isotopic labelling studies proved that Cu nanocubes which underwent a single oxidation-reduction presents an oxygen content lower than 1.0 at.%.[64] X-ray Photoelectron Spectroscopy (XPS) on Cu 2p cannot univocally distinguish Cu^+ from metallic Cu,[65] so no residual Cu_2O phase was ever reported through this technique.[66] Finally, some studies have discarded the existence of Cu_2O crystalline phases under CO_2 reduction conditions conditions.[61,62,67,68] The increase of ethylene selectivity on OD-Cu has then been explain solely through surface reconstruction toward open facets.[69,70] *Operando* electrochemical Scanning Tunnelling Microscopy (EC-STM) identified polycrystalline Cu (pc–Cu) reconstruction toward Cu(100) at potentials < -0.1 V vs. RHE[71], whilst High Resolution Transmission Electron Microscopy (HR-TEM) detected structural nanocubic rearrangements at $U < -1.1$ V vs RHE.[72] This massive restructuring have been attributed to surface polarization or reaction intermediates.[47,71–73]

S2.2 Oxygen stability in OD-Cu materials

To have a theoretical reference for oxygen stability, we probed the hydrogenation and desorption as water of 21 surface oxygen atoms randomly selected from our OD-Cu models. The net reaction was highly exothermic for half of the assessed sites and nearly thermoneutral for the other half. These results align with previous theoretical reports, where O was stable for a disordered Cu_xO_y matrix[74] and unstable in high ordered interstitial sites.[75,76] The potential and pH at which O desorption is exothermic was estimated from its Gibbs free energy and applying the computational hydrogen electrode approach,[22] **Equations S23-S24**, and it is shown in **Figure S4**.

$$Cu_xO_y + 2H^+ + 2e^- \rightarrow Cu_xO_{y-1} + H_2O; \Delta G_{\text{O-des}} \tag{S23}$$

$$U_{\text{O-des}} = \frac{1}{2e^-}(\Delta G_{\text{O-des}} + k_B T \ln 10 \cdot \text{pH}) \tag{S24}$$

Under electrochemical CO_2R conditions, pH is typically alkaline nearby the catalyst surface.[77–80] COMSOL simulations of micro-sized copper cavities accounted for a surface pH of 10,[81] value which was calculated as well solving diffusion and electrostatic equations numerically at cathodic current densities of 10 mA cm^{-2}.[82] Experimental determinations of surface pH *via* a IrO_x ring detector on a Au rotating disk estimate an increase of 4.5 units per order of magnitude of current densities in the range 10-100 mA cm^{-2}.[83] Assuming a surface pH of 10 (14), more than half of our O configurations are reported stable for electric potentials ~ -0.3 (-0.6) V vs RHE and their stability window extends until -0.64 (-0.84) V vs RHE. Therefore, due the stabilization given by the high surface pH, we can confirm the presence of residual oxygens at those low potentials where OD-Cu catalysts proved outstanding CO_2 reduction activity and ethanol selectivity,[84] from -0.3 to -0.6 V vs RHE. Contributions of configuration entropy which we did not include here may extend further the stability region of the residual oxygens.[27,34] Previous reports on oxides assessed the contribution of configurational entropy stabilization by around 0.2 eV[27]. Conversely, the uncertainty in estimation of surface pH by at least 2 units sets the lower limit of oxygen stability to -0.6 V vs RHE. Taking both these contributions into account, we conclude that residual oxygens are thermodynamically and kinetically stable on OD-Cu until -0.6 al low surface pH or -1.0 V vs RHE due to configurational entropy. Our results agree with the recent experimental evidence of oxygen in a $Cu(OH)_2$-derived catalyst at -1 V vs RHE motivated by the detecttion of Cu-O EXAFS peak[52]. Yet, our prediction on the extent of residual oxygen at a given pH and potential is qualitative because of the limited sampling of oxygen configurations. Variations of electrolyte dielectric permittivity under CO_2 reduction conditions did not influence oxygen stability, as theoretically proved by comparing solvation effects at $\epsilon_r = 78.5$ and $\epsilon_r = 50.0$,[82] **Figure S26**.

S3 Figures

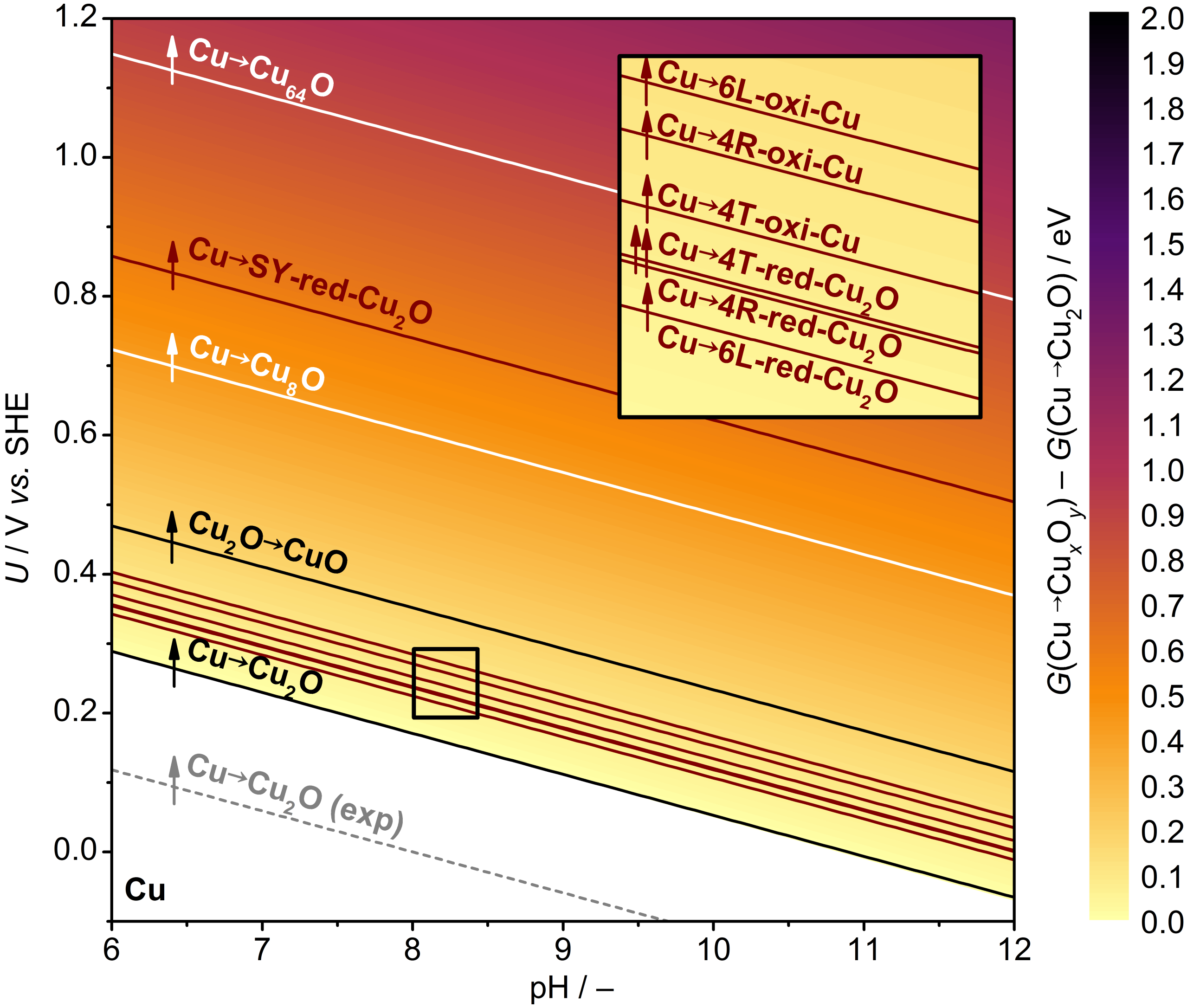

Figure S1: Surface Pourbaix diagrams for OD-models. For the Cu-O at neutral pH and mild potential, the thermodynamically stable phases are Cu, Cu_2O, and CuO (black lines). Experimentally identified Cu_8O and $Cu_{64}O$ metastable phases are less stable than Cu_2O by 0.43 and 0.86 eV respectively,[31,32] white lines, **Table S7**. Red-Cu_2O and oxi-Cu systems have formation energies within 0.10 eV from Cu_2O, with the exception of SY-red-Cu_2O, dark red lines, **Tables S6**. As reference, we reported in gray the transition between bulk Cu and Cu_2O from experimental values,[26] in agreement with our DFT benchmark for bulk copper oxide, **Table S18**.

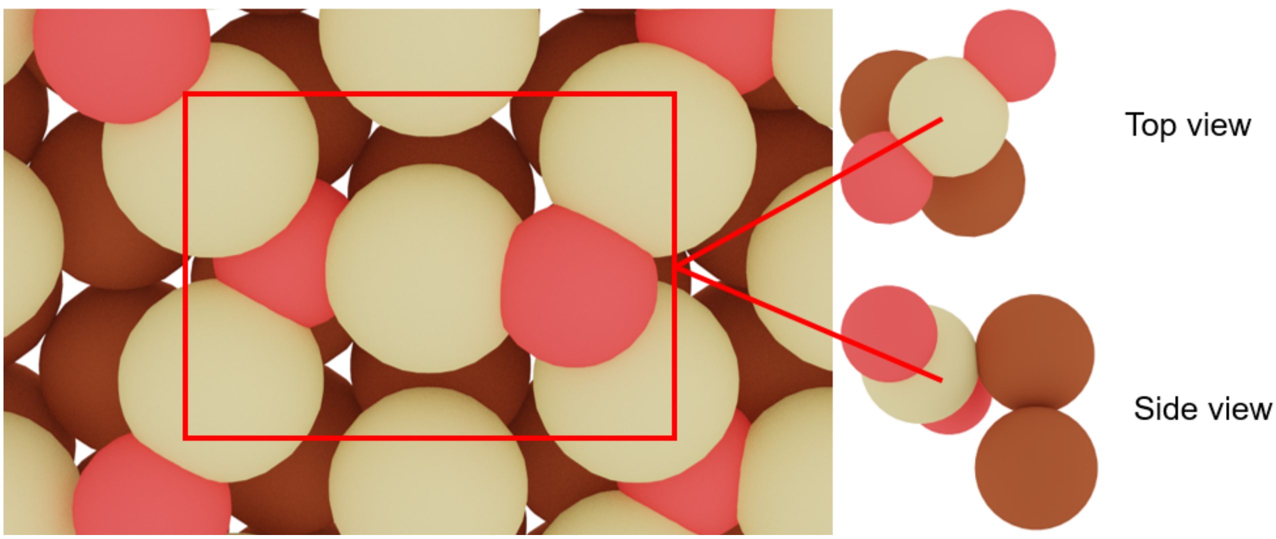

Figure S2: Cu/Cu_2O grain boundary. The Cu/Cu_2O interface reduces the surface energy of the Cu metal phase remarkably more than a suboxide phase.[44] This ensemble is more likely to occur inside the material than at the most external layer.[44] We provide here a close view of a typical grain boundary configuration for Cu/Cu_2O interface prior to *ab initio* molecular dynamics. This pattern is stable and forms widely without the presence of a defined Cu_2O crystalline structure, see **Supporting Discussion**.

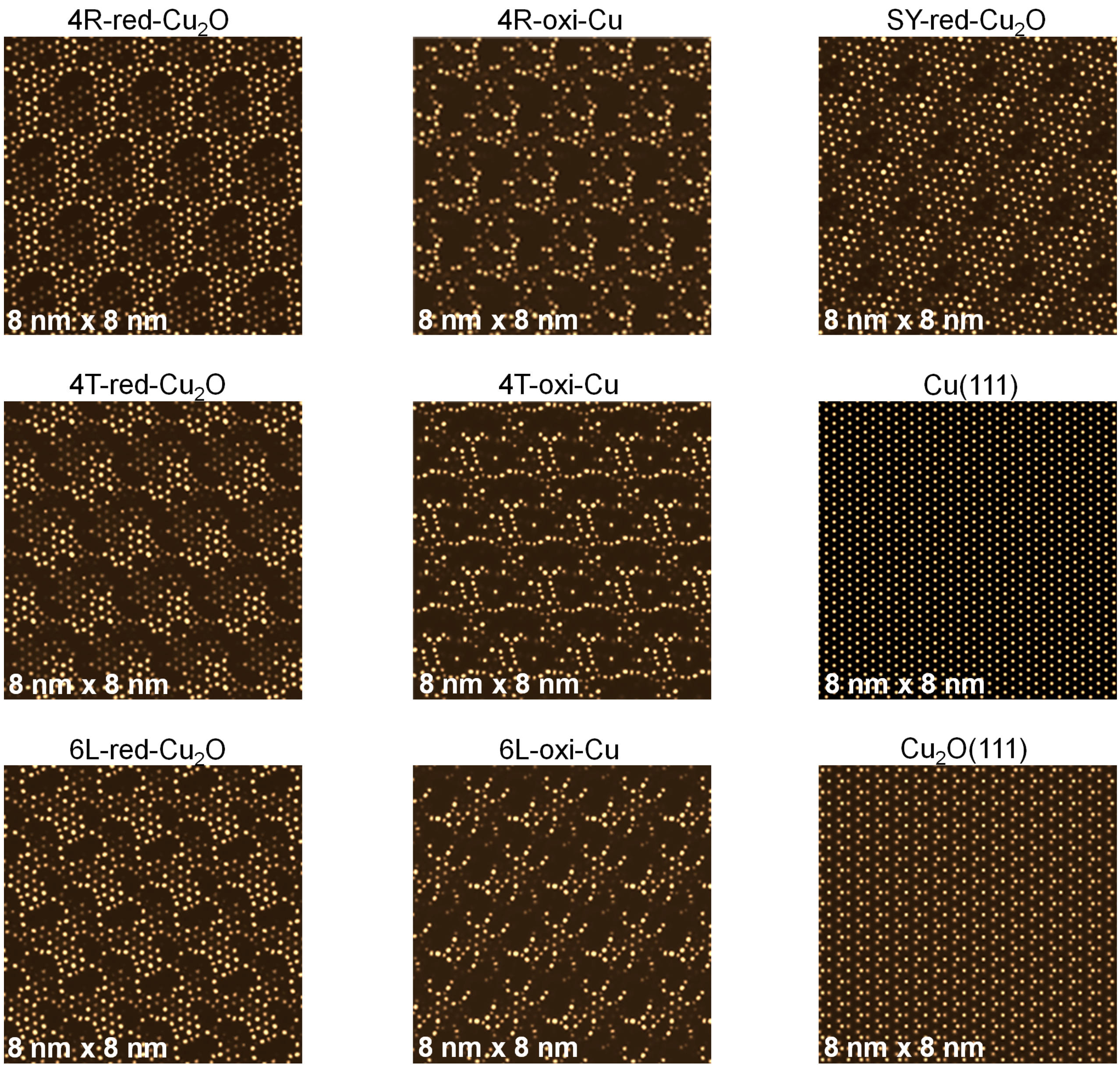

Figure S3: STM characterization for OD-models. We simulated Scanning Tunneling Microscope (STM) images for red-Cu_2O and oxi-Cu final configurations, setting the tip at constant height. As a reference, we included as well STM characterization of crystalline Cu(111) and $Cu_2O(111)$. Image size and tunnelling parameters are: $A = 8 \times 8$ nm^2 and $V_s = -1.0$ V vs ϵ_F. The reconstructed structures resemble experimental characterization for autocatalytic reduction of Cu_2O from CO adsorption.[85]

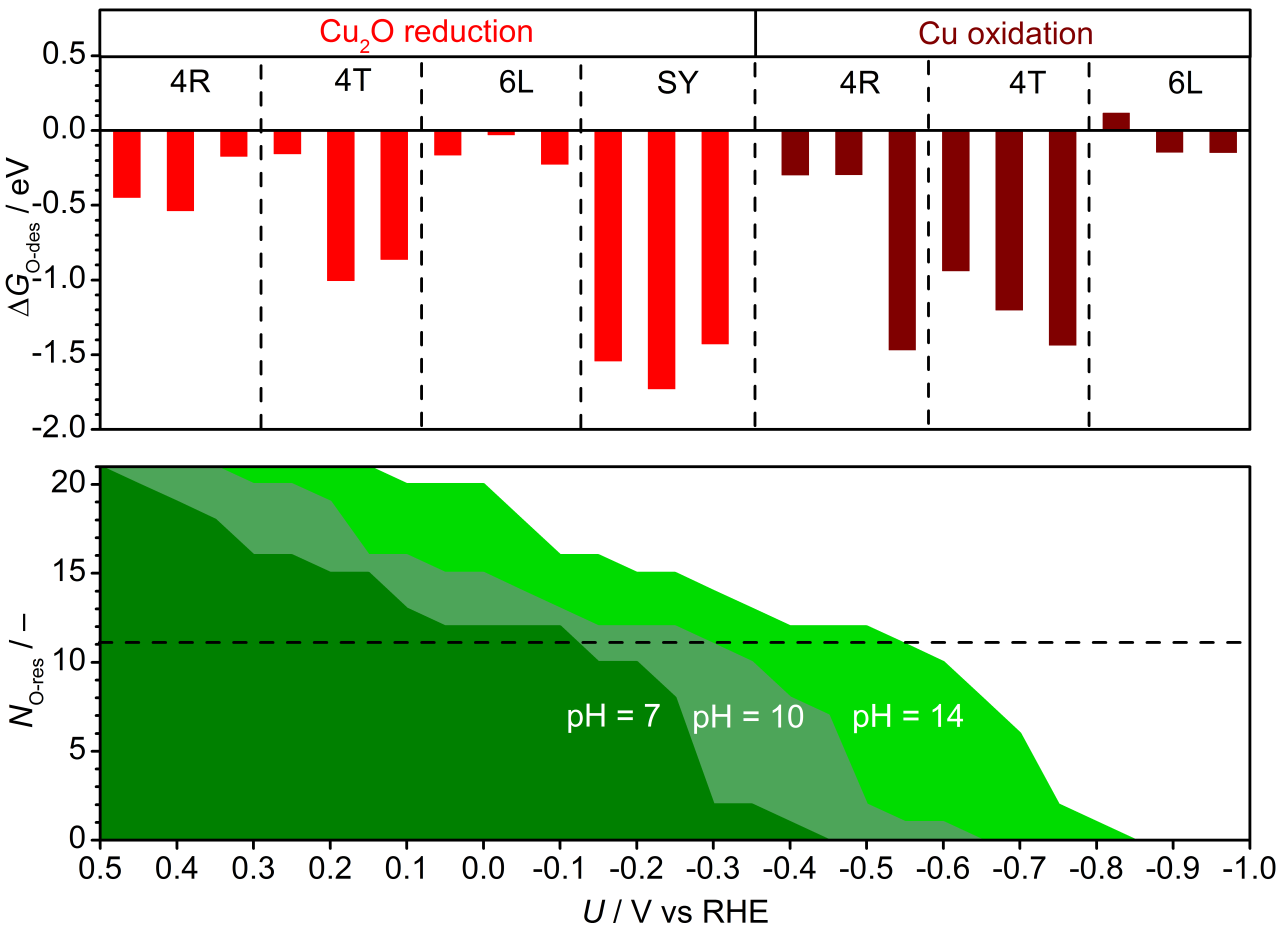

Figure S4: Oxygen stability. We sampled 21 surface and subsurface oxygens to assess O desorption as a water molecule. O desorption was reported exothermic for almost all the configurations assessed, $\Delta G_{\text{O-des}} < 0$ eV (**Equation S23**). However, for alkaline pHs (ligh green) expected for electrochemical CO_2 reduction,[77–83] residual oxygens are reported stable until -0.84 V vs RHE. Remarkably, the stability window includes the potential range where OD-Cu catalysts proved outstanding CO_2 reduction activity and C_{2+} selectivity.[84]

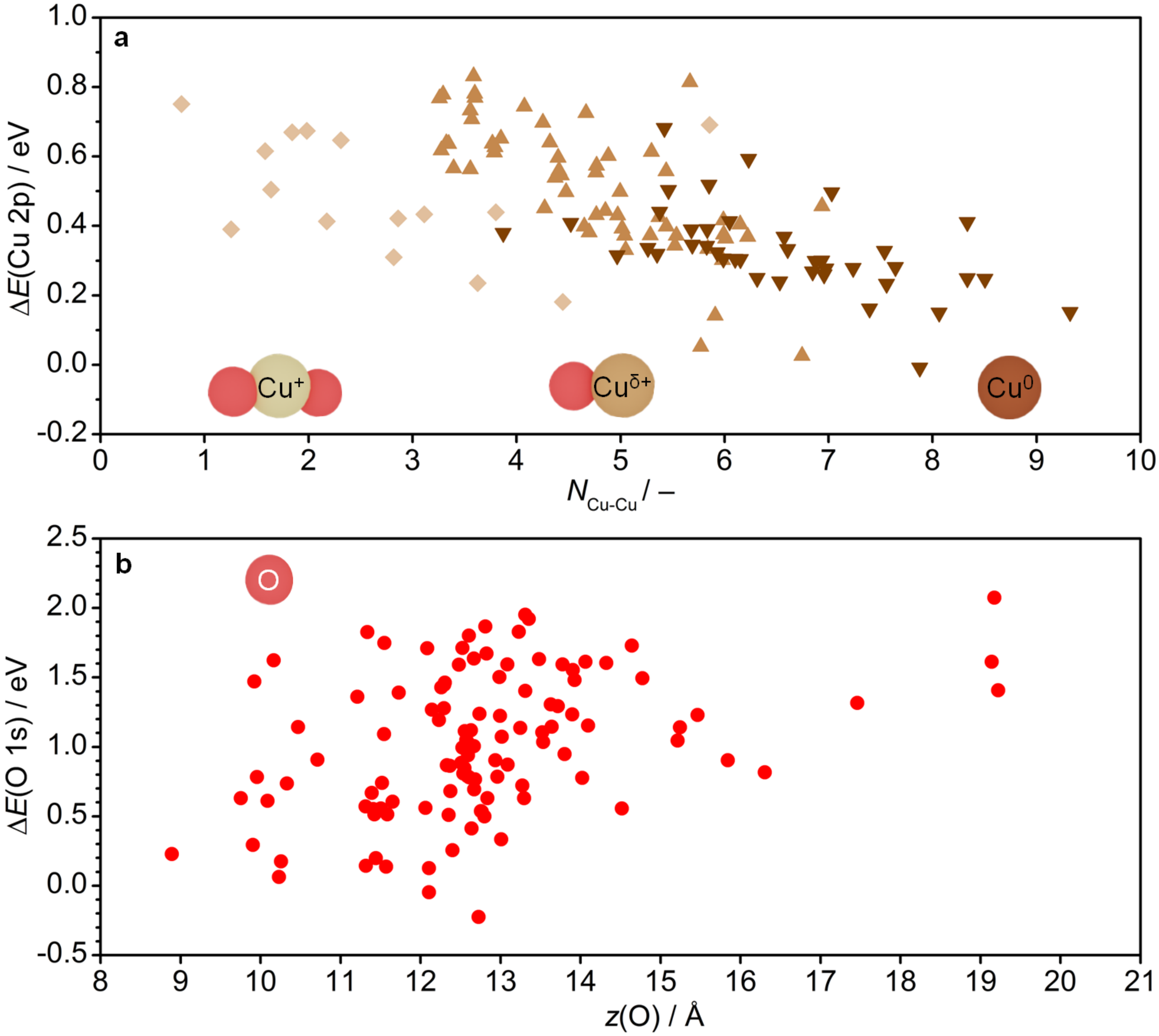

Figure S5: XPS shifts for Cu 2p and O 1s for OD-Cu models. **a**, $Cu^{\delta+}$ (Cu^+) atoms presents a positive shift of the Cu 2p XPS peak (vs Cu 2p for crystalline Cu) due to their higher oxidation state. Cu 2p XPS peak for low coordinated Cu^0 sites denotes as well a positive shift, whilst higher coordination sites resembles crystallline Cu. The estimated shifts are within the range reported in literature for OD-Cu catalysts, $\sim$ 0.5 eV.[51] **b**, O 1s XPS peak (vs O 1s for Cu_2O) shows a significant positive shift due to the lower electronic density on the resulting atoms. Sites characterized by $\Delta E \sim 2$ eV are attributed to adventious O species[51], whilst $\Delta E \sim 1$ eV to O adatoms.[45] Few negative shifts are fingerprint for subsurface O.[45]

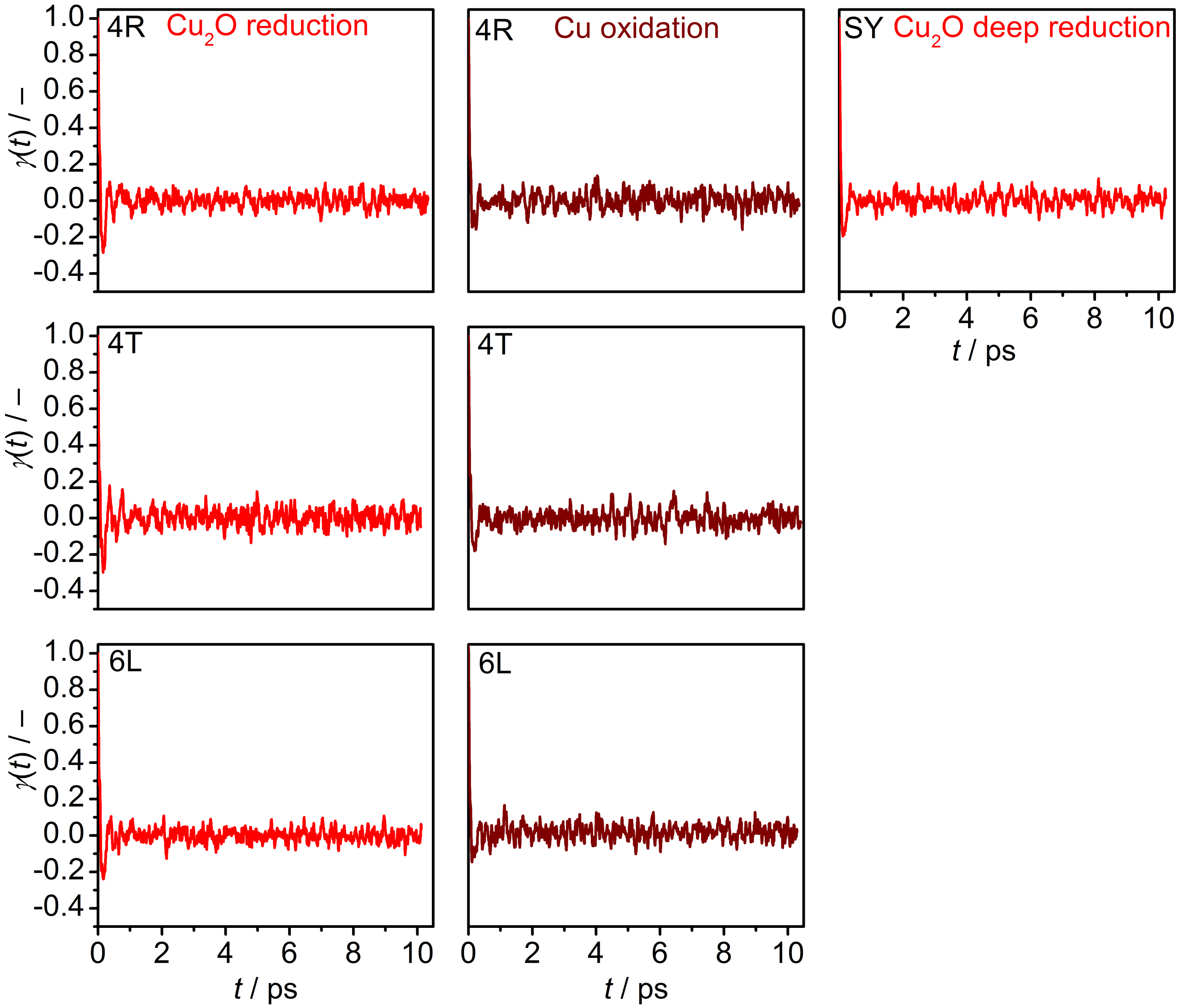

Figure S6: Velocity Autocorrelation Functions for OD-models. As defined by **Equation S11**.

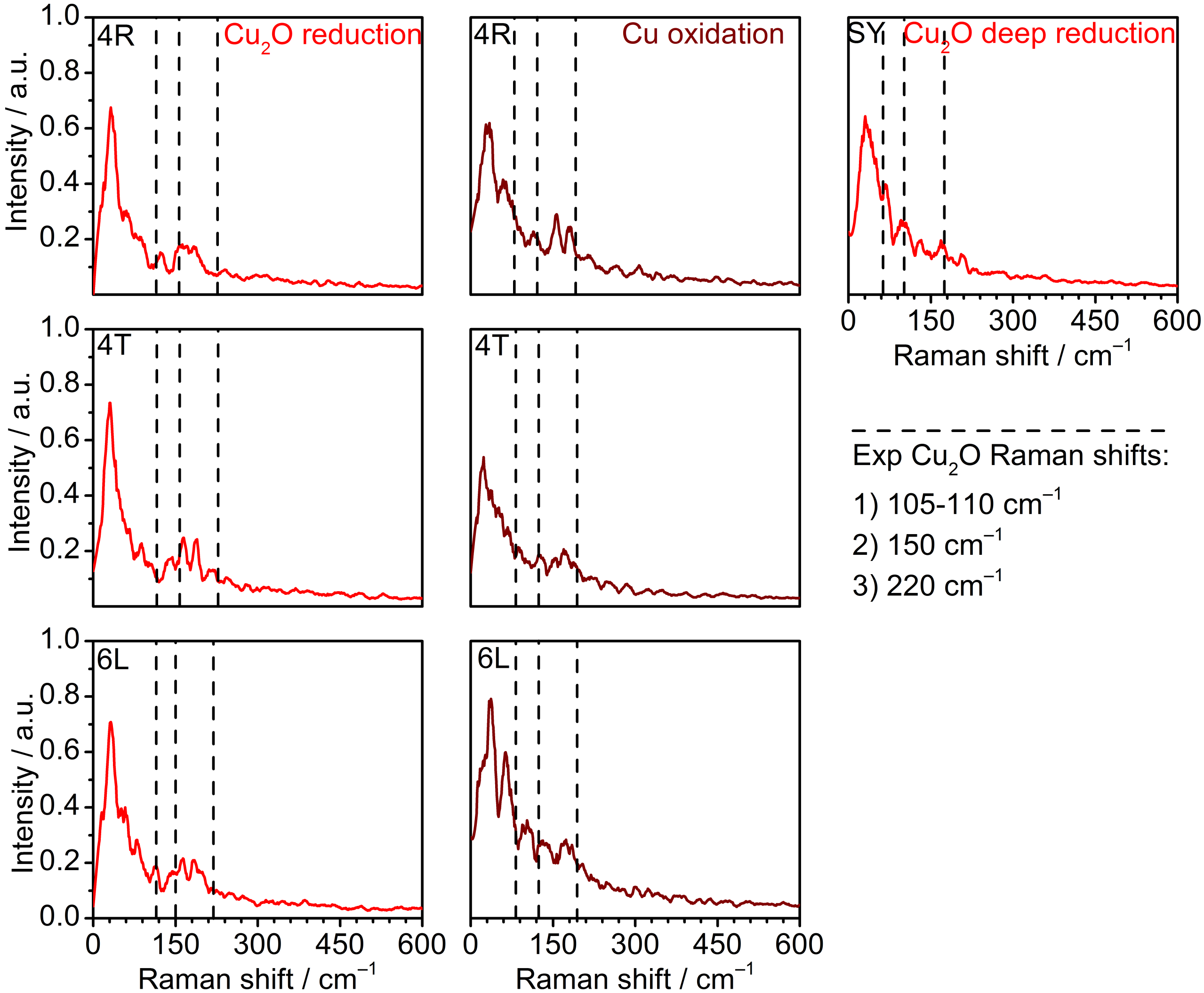

Figure S7: Raman shifts for OD-models. Computed from a Discrete Fourier transform from data in **Figure S6** as defined in **Equation S12**. A digital Savitzky-Golay filter was applied to smoothing the function, fitting 20 adjacent points with a polinomial orders of grade 2. Dashed lines represent relevant vibration frequencies reported experimentally for Cu_2O and OD-Cu.[67,86,87] We could not observe the peaks assigned to $CuO_x(OH)_y$ ($\sim$ 390, $\sim$ 530 cm^{-1}) and Cu-O_{ads} ($\sim$ 600 cm^{-1}),[87] since we did not include explicit solvation in our AIMD simulations and the relative abundance of O_{ads} species was low (**Figure S22**).

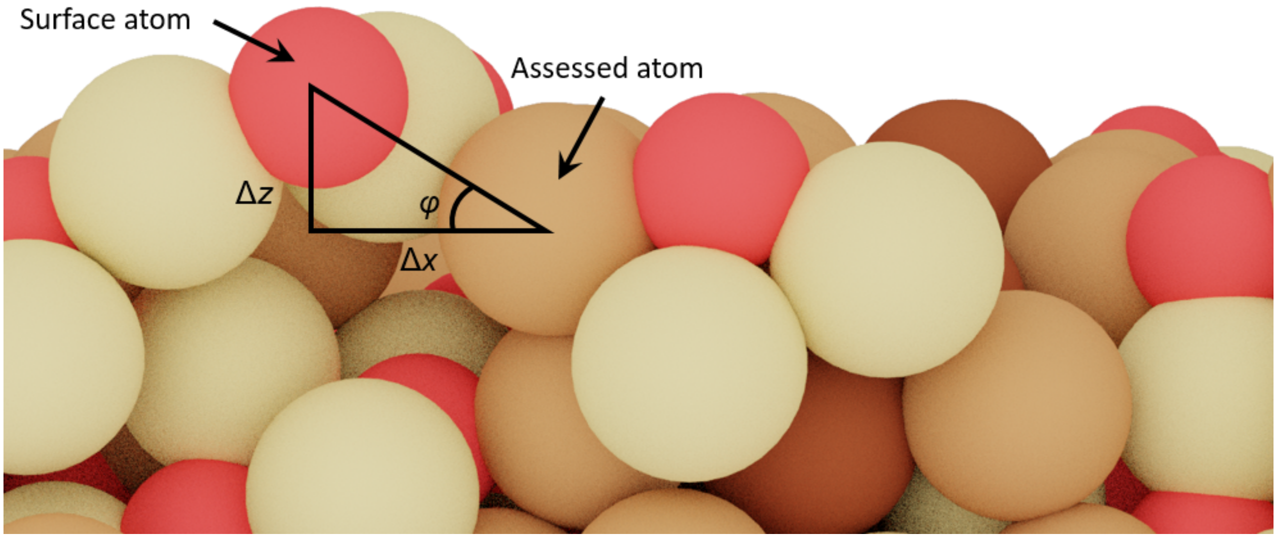

Figure S8: Definition of surface atoms. Angle φ as defined by **Equation S14** in a 2D projection. A assessed atom is defined a surface atom if the angles with any previously determined surface atoms ϕ is smaller than 50 degrees.

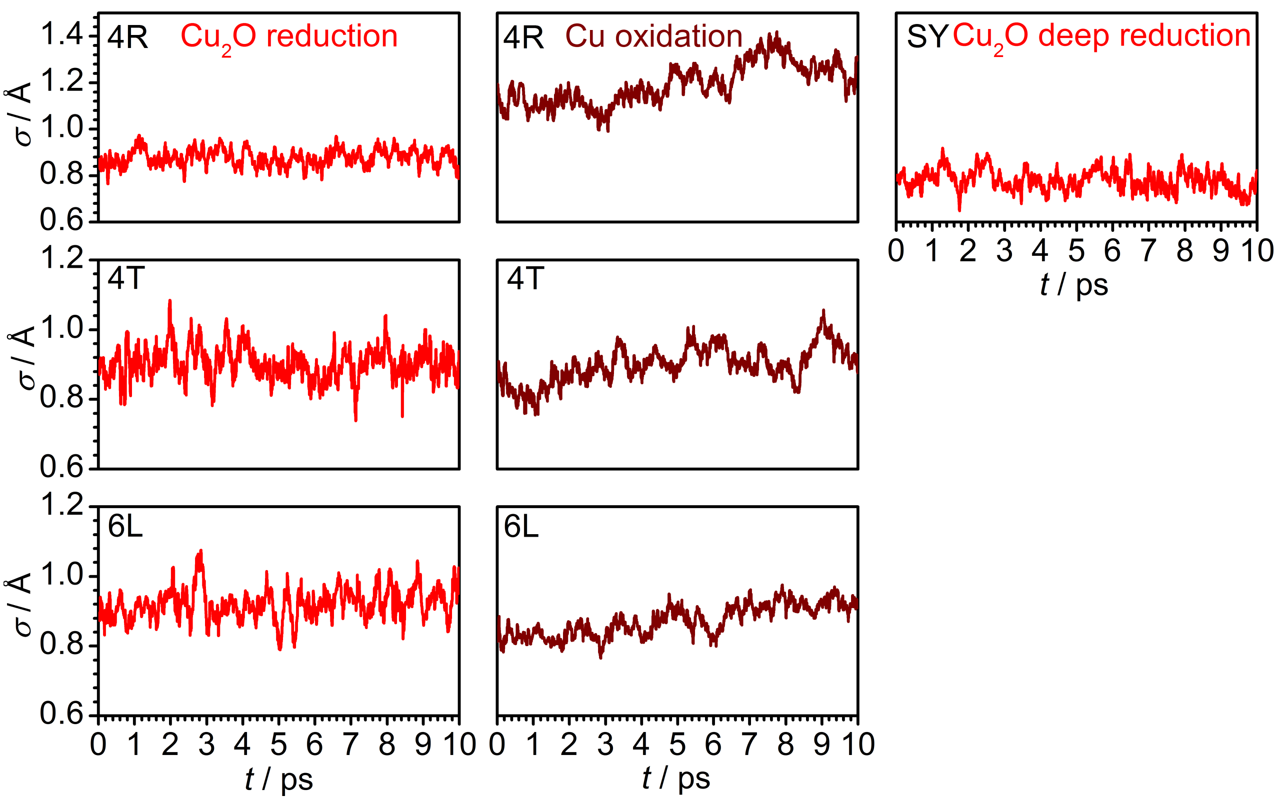

Figure S9: Surface roughness. As calculated by **Equation S15**.

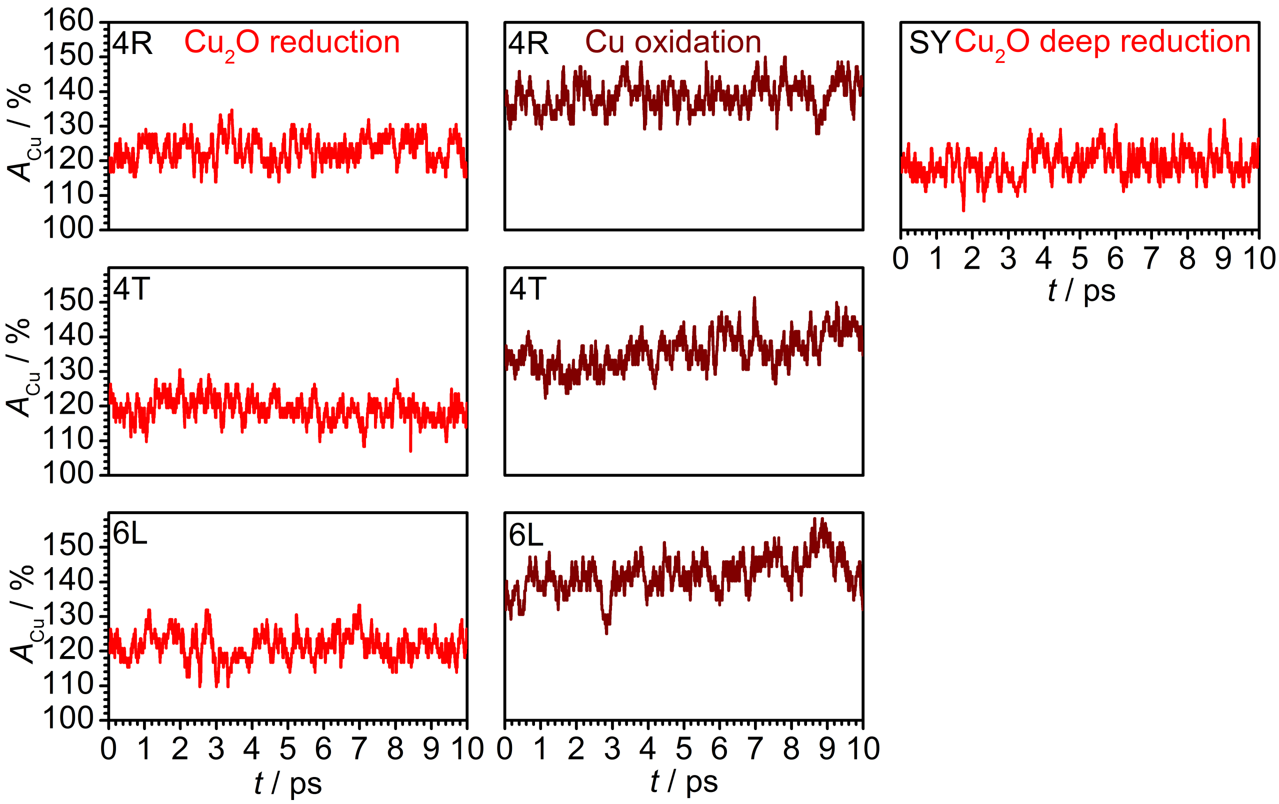

Figure S10: Surface activity. As described by **Equation S16**.

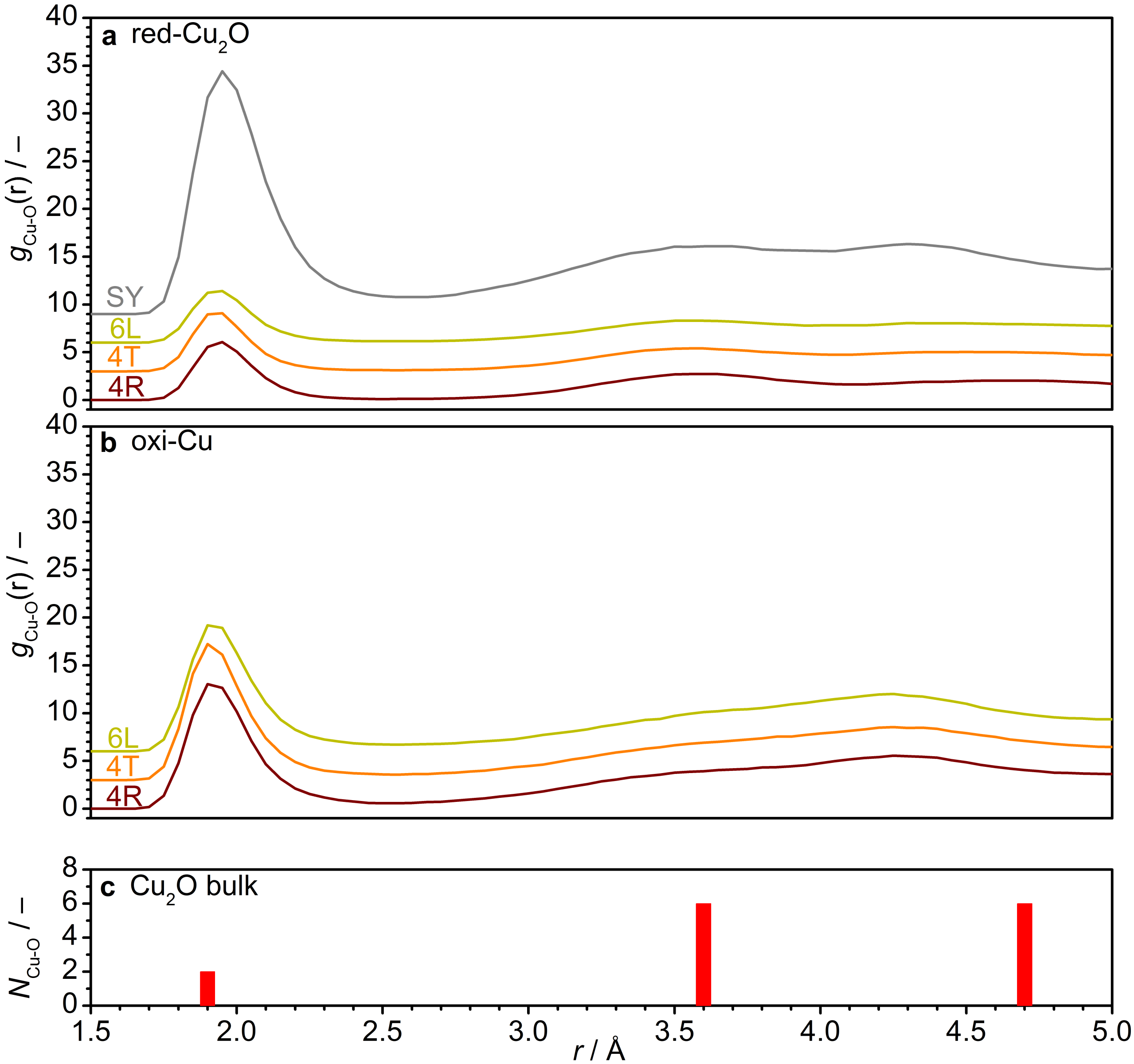

Figure S11: Cu-O radial distribution function. a-b, red-Cu_2O and oxi-Cu systems. **c**, crystalline Cu_2O.

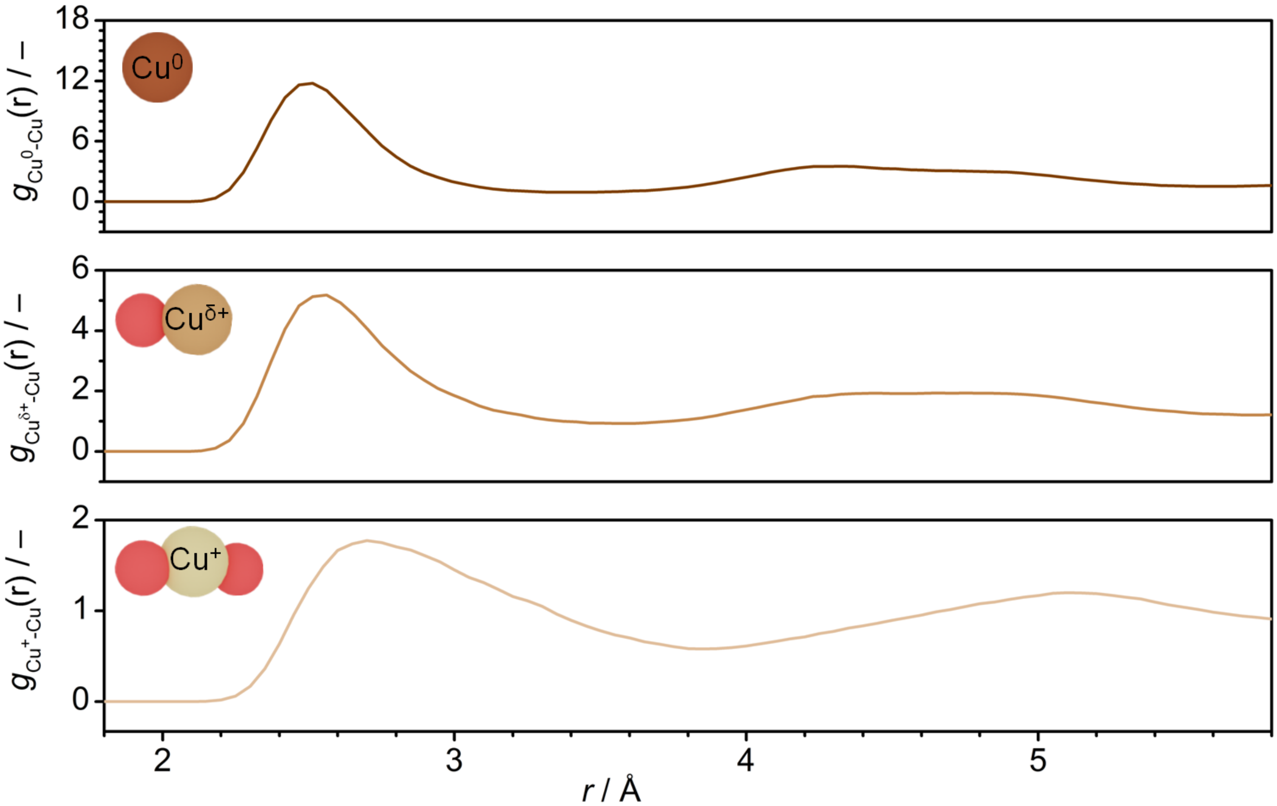

Figure S12: Cu-Cu radial distribution functions for SY-red-Cu_2O.

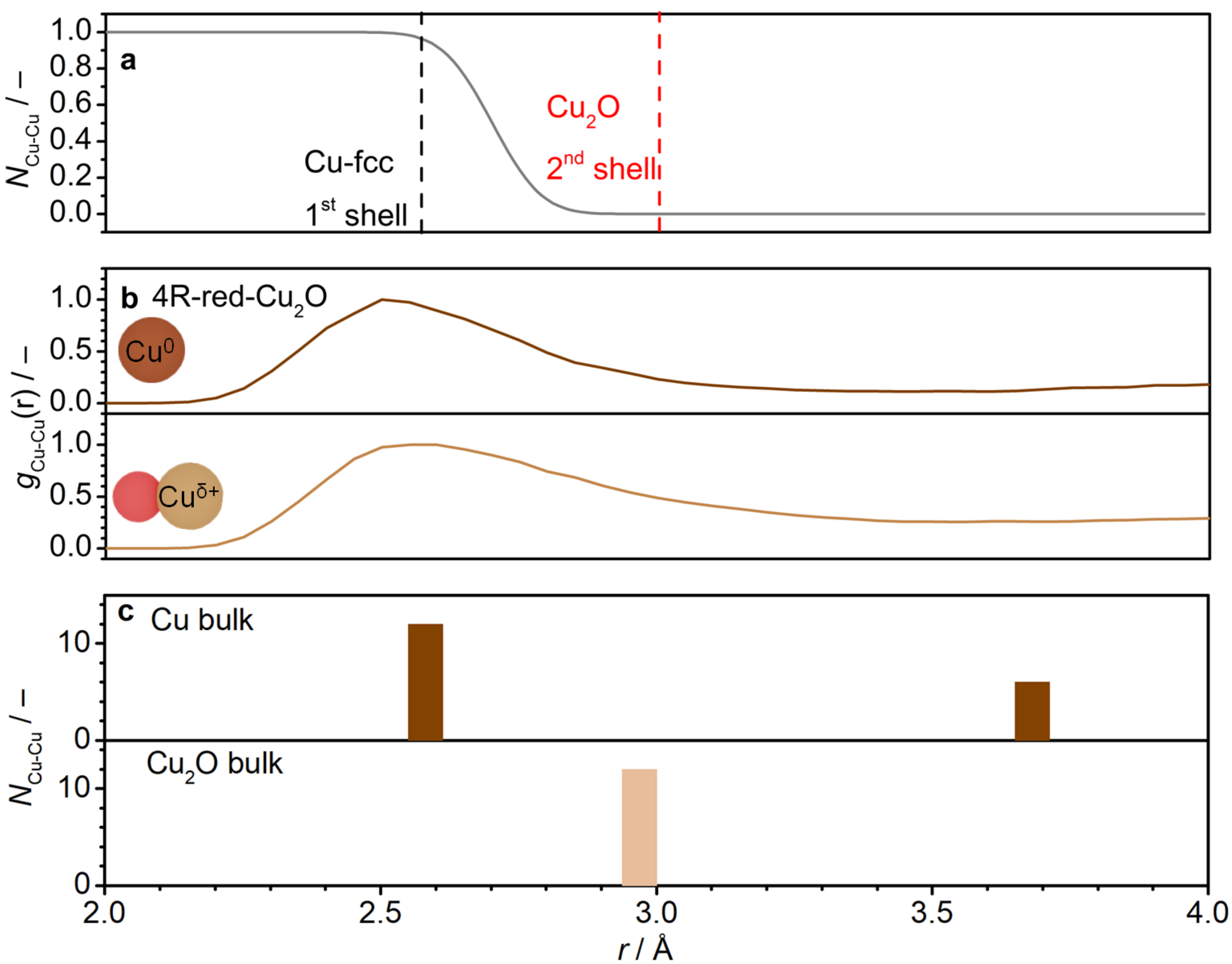

Figure S13: Cu-Cu coordination shells. **a** Decay between the first and second Cu-Cu coordination shell. **b-c**, given the interplay between first Cu coordination shell and second Cu_2O coordination shell, we listed Cu-Cu coordination numbers employing the continuous function, **a**, derived in **Equation S19**.

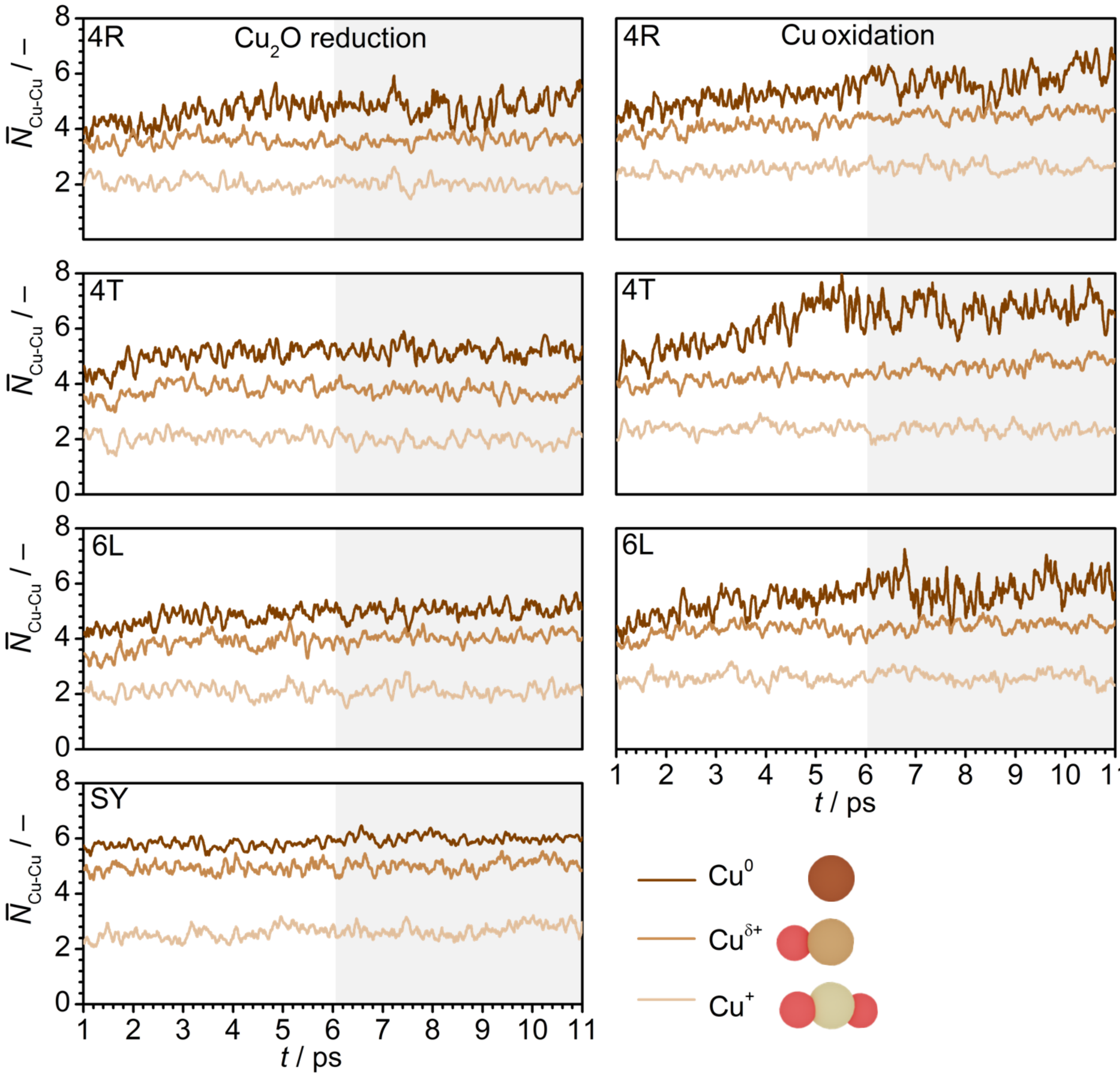

Figure S14: Evolution of average Cu-Cu coordination number for Cu^0, $Cu^{\delta+}$, and Cu^+. Cu-Cu coordination numbers, $N_{\text{Cu-Cu}}$, were calculated from **Equation S19**. The averaged value $\overline{N}_{\text{Cu}-\text{Cu}}$ for the final 5 ps (gray area) is reported on **Table S8**.

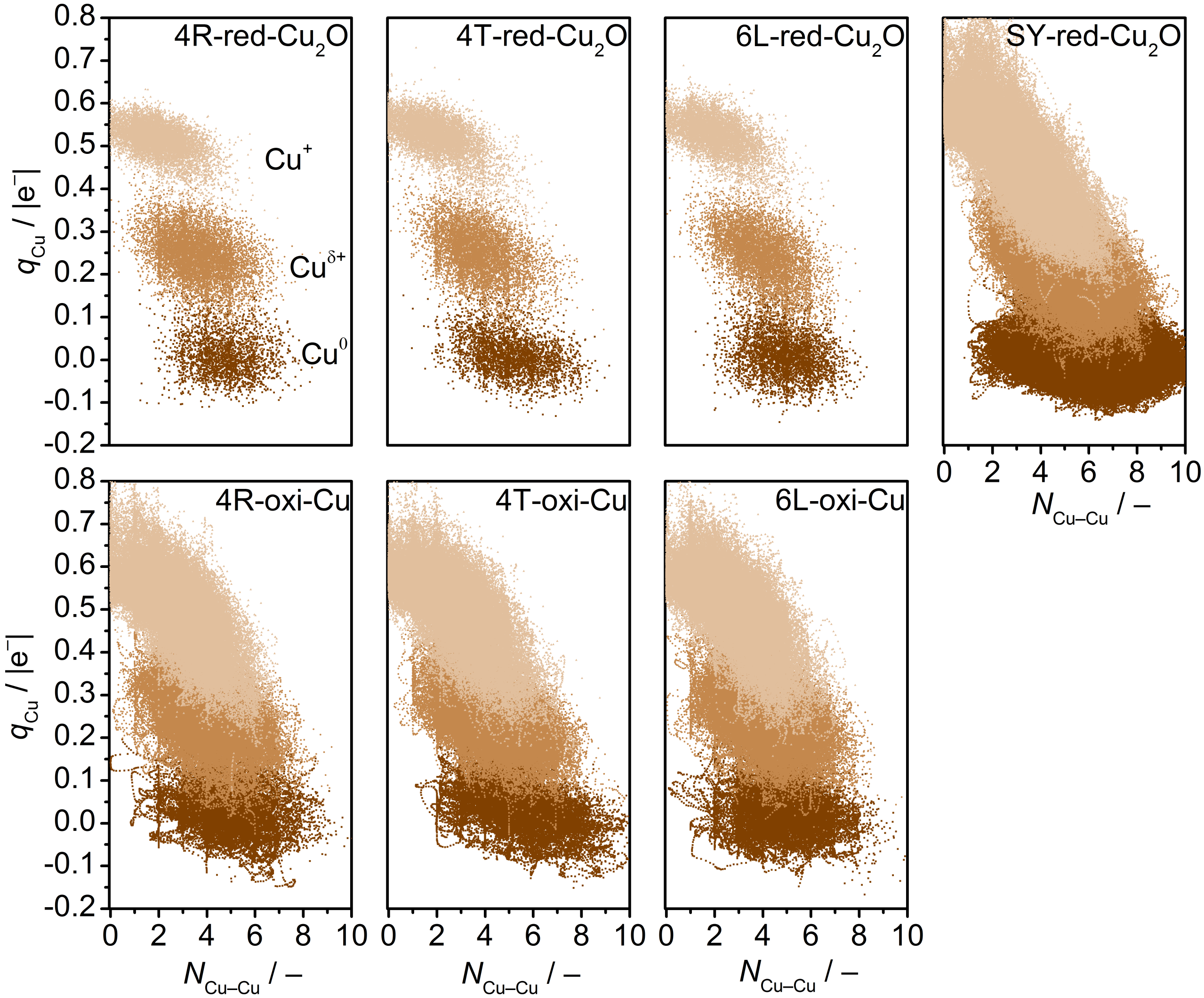

Figure S15: Cu-Cu coordination number vs Cu Bader charges. Cu-Cu coordination numbers, $N_{\text{Cu-Cu}}$, were calculated through **Equation S19**. For both red-Cu_2O and oxi-Cu models, we detected three Cu species: Cu^0, $Cu^{\delta+}$, and Cu^+ at $q_{\text{Cu}} \sim 0$ $|e^-|$, $0.1 \leq q_{\text{Cu}} \leq 0.4$ $|e^-|$, and $q_{\text{Cu}} \geq 0.4$ $|e^-|$, respectively.

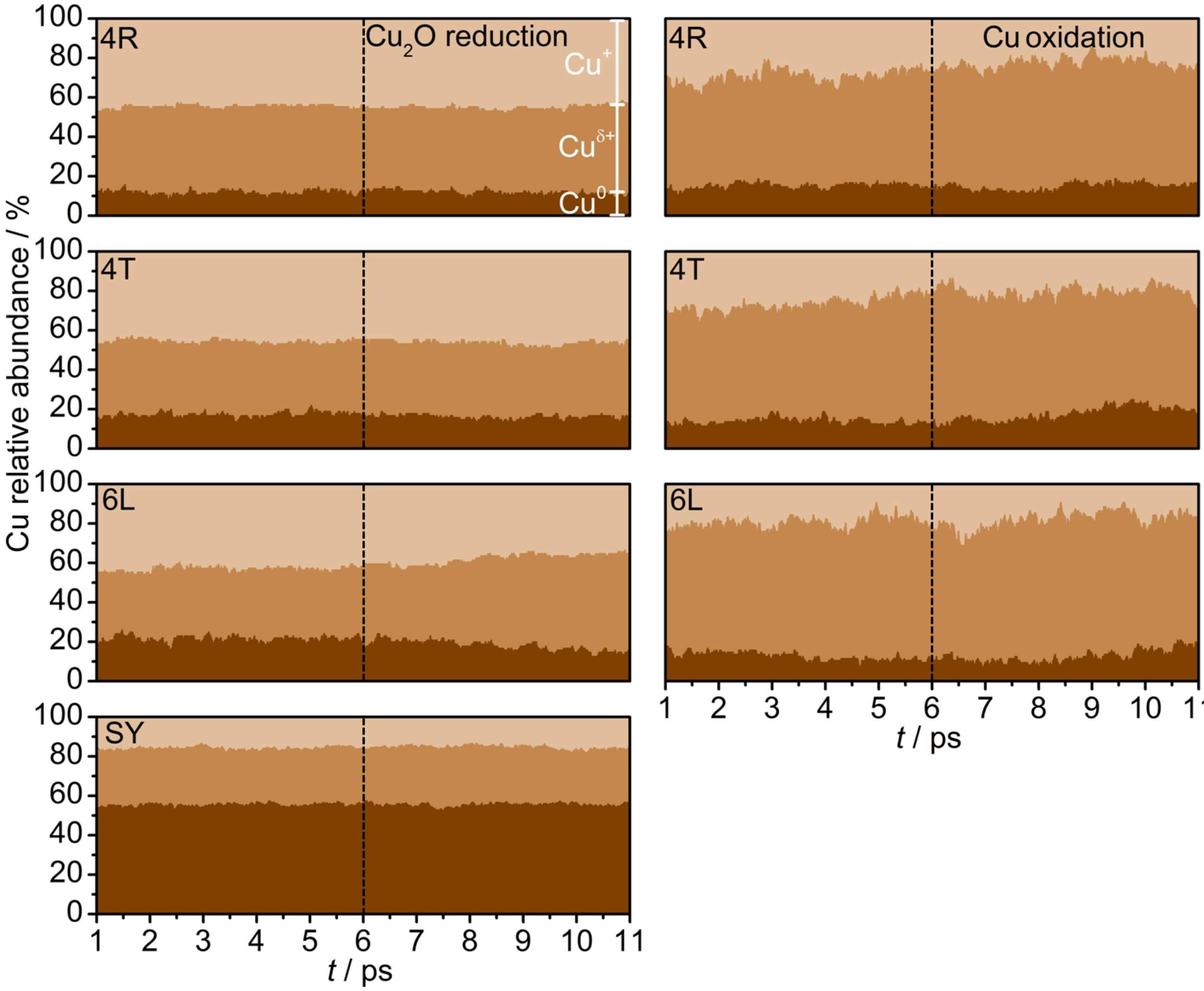

Figure S16: Relative abundance of Cu species over time. For both red-Cu_2O and oxi-Cu, Cu species evolution does not change significantly over time. Red-Cu_2O are characterized by low amount of Cu^0 sites ($\sim 10 - 20\%$) and around 50% of oxidic phases still persistent. Oxi-Cu systems are more disordered due to the stress at the interface Cu(111)/Cu_2O(111). Therefore, $Cu^{\delta+}$ abundance accounts for 50% of the total Cu sites. Deep Cu_2O reduction conditions, SY-red-Cu_2O, determine a strong presence of metallic Cu, 50-60%. We computed averaged abundances after a stabilization period of $\Delta t = 6$ ps, dashed line, and reported them in **Table S9**.

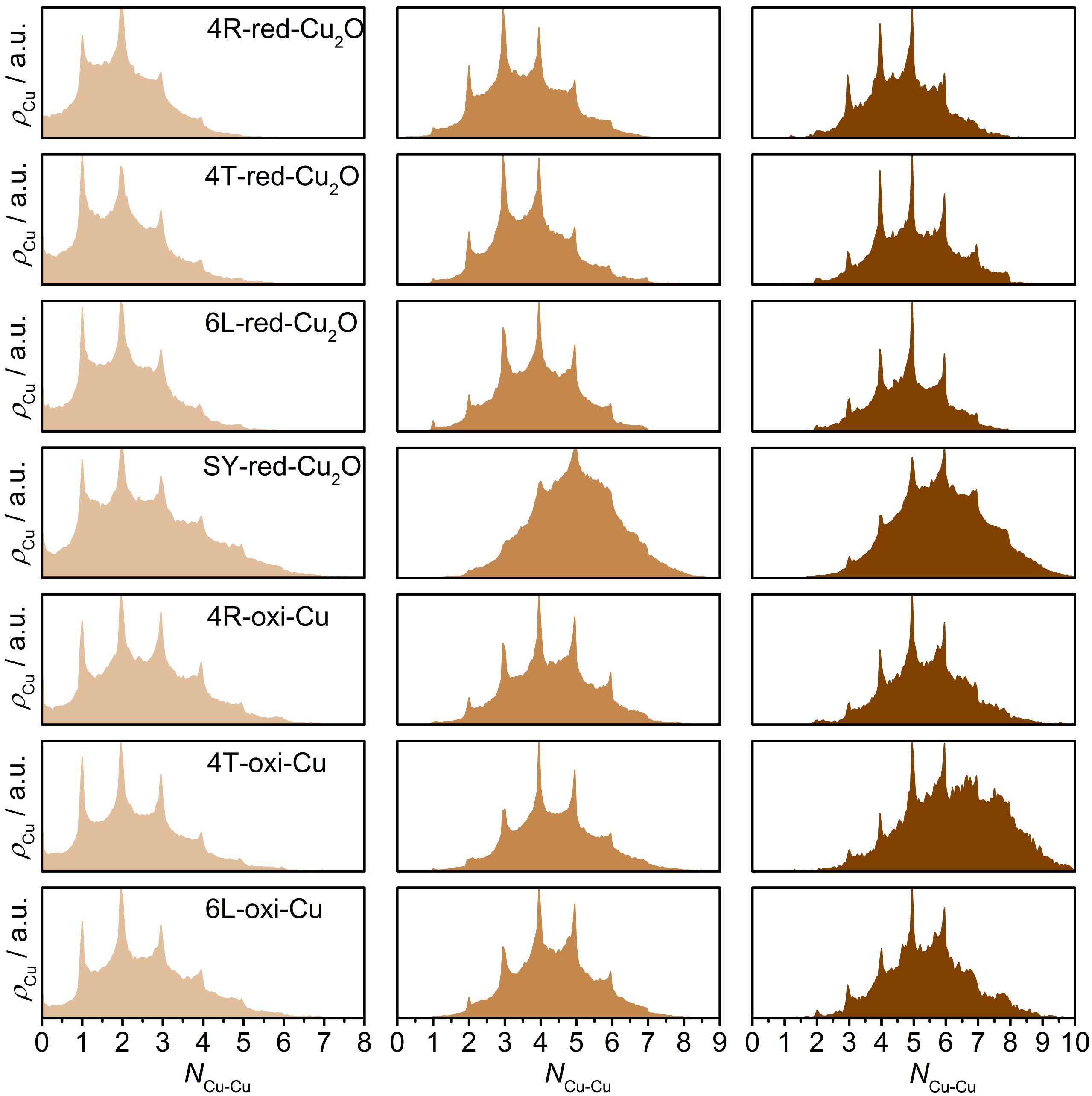

Figure S17: Cumulative maps of Cu-Cu coordination number. Both red-Cu_2O and oxi-Cu systems display higher densities at integer $N_{\text{Cu-Cu}}$ coordinations, therefore suggesting the presence of stable and recurrent ensembles.

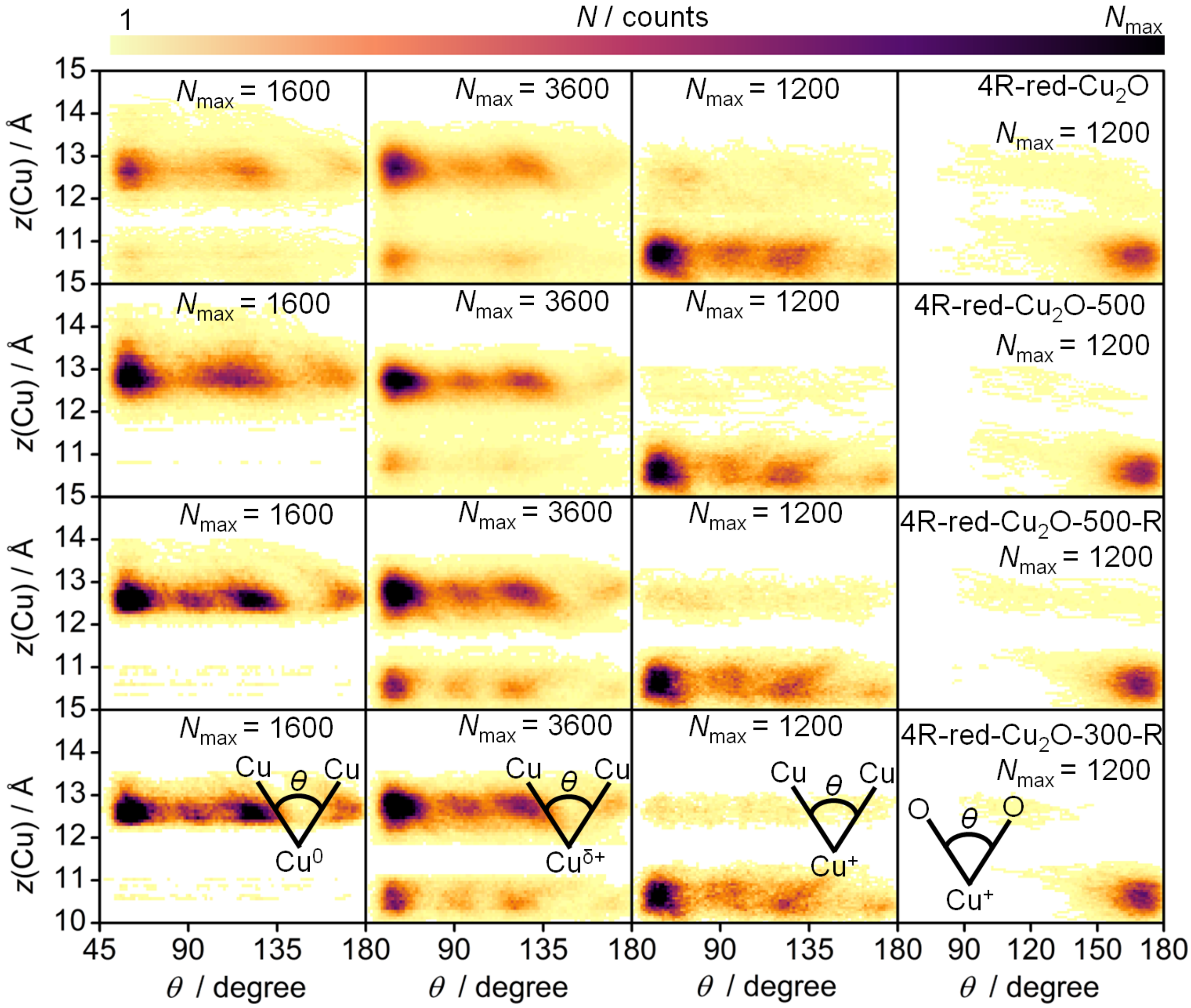

Figure S18: Benchmark for AIMD temperature: Histograms for angles θ(Cu − Cu^0 − Cu), θ(Cu − Cu$^{\delta+}$ − Cu), θ(Cu − Cu$^+$ − Cu) and θ(O − Cu$^+$ − O) at different heights z(Cu). 4R-red-Cu_2O: 1 + 10 ps AIMD at 700 K. 4R-red-Cu_2O-500: 1 + 10 ps AIMD at 500 K. 4R-red-Cu_2O-500-R: 2.0 ps AIMD ramp from 700 K to 500 K + 4.5 ps AIMD stabilization at 500 K. 4R-red-Cu_2O-300-R: 2.0 ps AIMD ramp from 700 K to 500 K + 2.0 ps AIMD ramp from 500 K to 300 K.

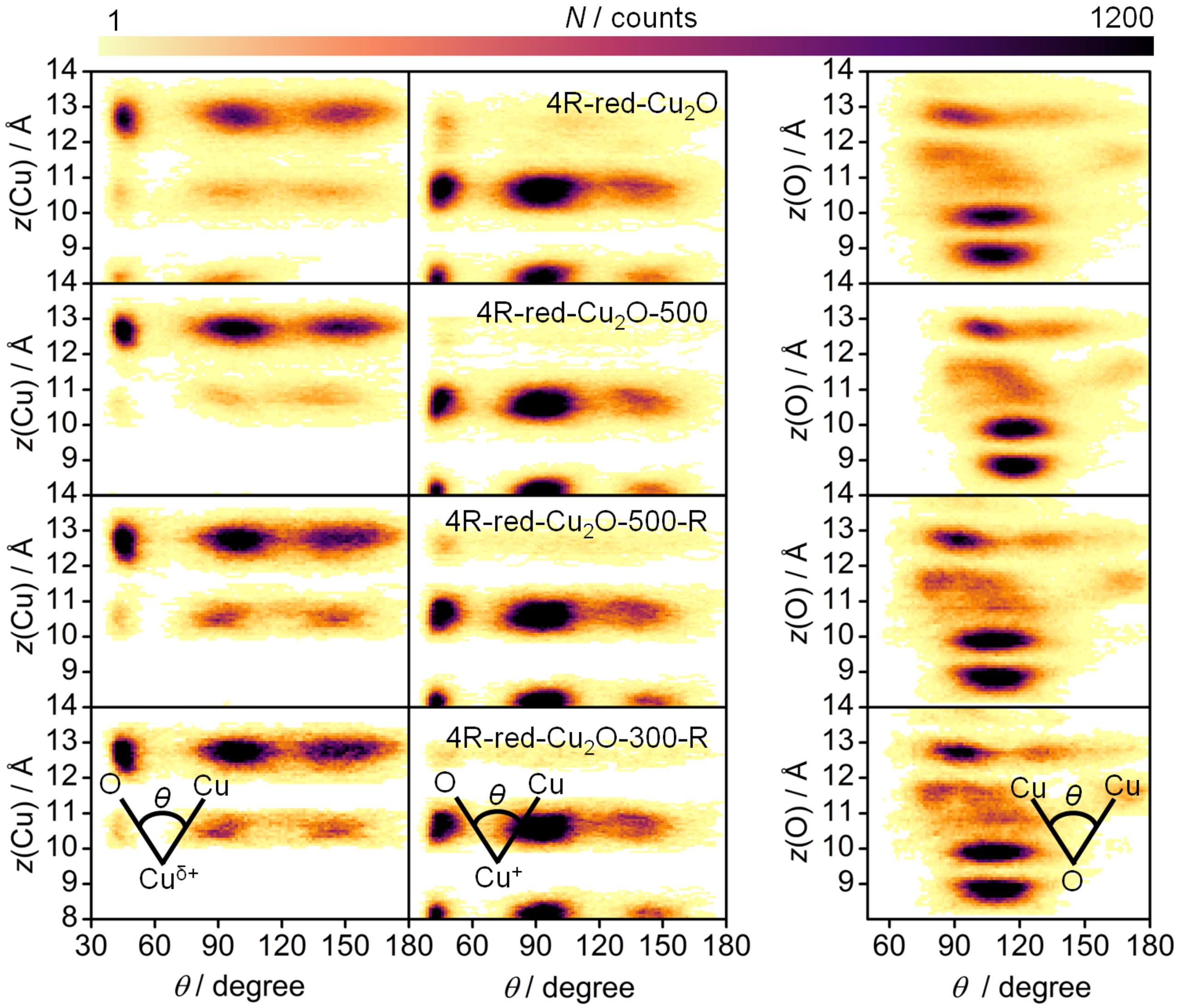

Figure S19: Benchmark for AIMD temperature: Histograms for angles θ(O – Cu$^{\delta+}$ – Cu), θ(O – Cu^{+} – Cu) and θ(Cu – O – Cu) at different heights z(Cu). 4R-red-Cu_2O: 1 + 10 ps AIMD at 700 K. 4R-red-Cu_2O-500: 1 + 10 ps AIMD at 500 K. 4R-red-Cu_2O-500-R: 2.0 ps AIMD ramp from 700 K to 500 K + 4.5 ps AIMD stabilization at 500 K. 4R-red-Cu_2O-300-R: 2.0 ps AIMD ramp from 700 K to 500 K + 2.0 ps AIMD ramp from 500 K to 300 K.

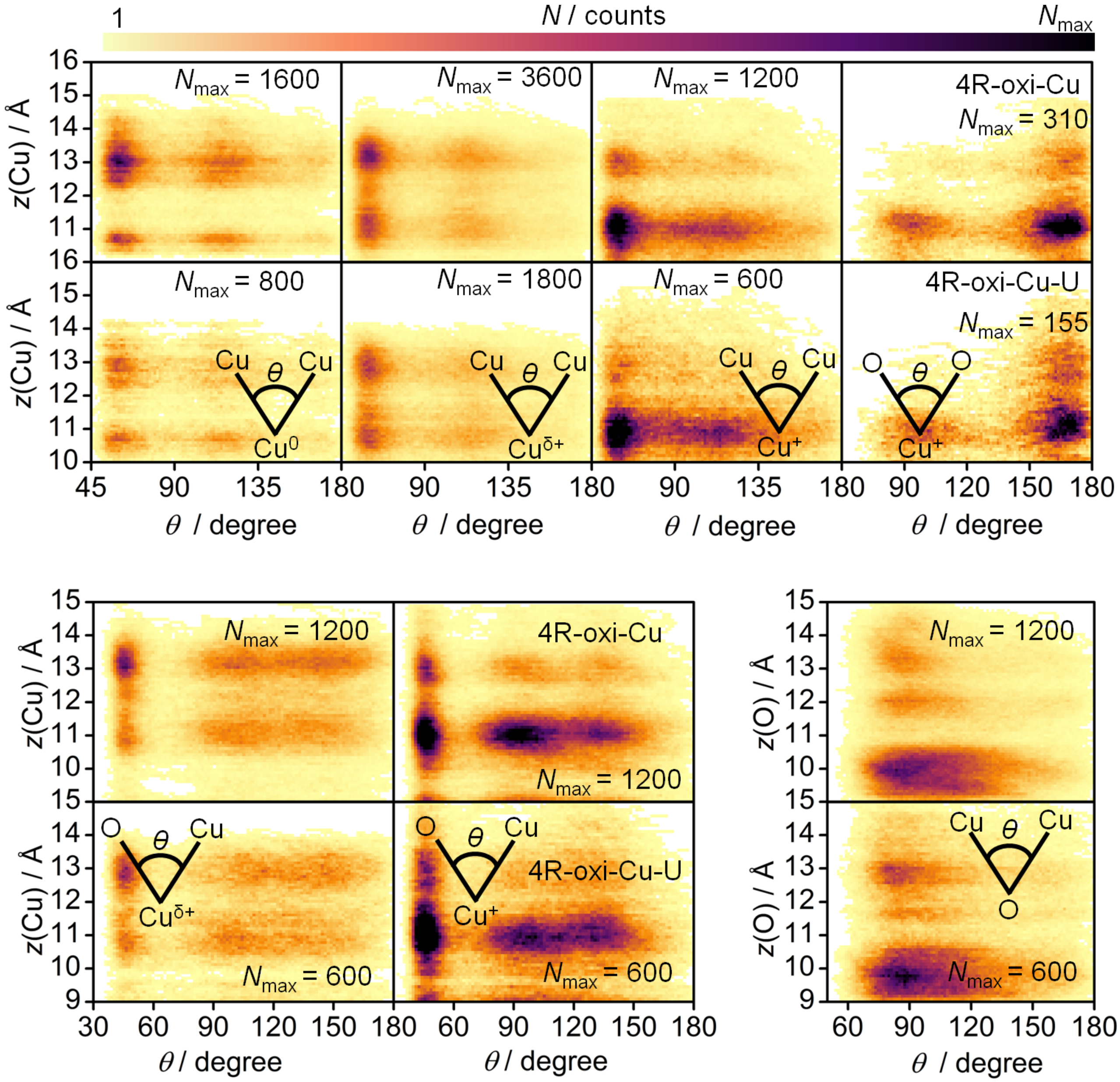

Figure S20: Benchmark for Hubbard correction: Histograms for angles $\theta(\mathbf{Cu-Cu^0-Cu})$, $\theta(\mathbf{Cu-Cu^{\delta+}-Cu})$, $\theta(\mathbf{Cu-Cu^+-Cu})$, $\theta(\mathbf{O-Cu^+-O})$, $\theta(\mathbf{O-Cu^{\delta+}-Cu})$, $\theta(\mathbf{O-Cu^+-Cu})$ and $\theta(\mathbf{Cu-O-Cu})$ at different heights $z(\mathbf{Cu})$. 4R-oxi: 1 + 10 ps AIMD at 700 K and no Hubbard correction. 4R-oxi-Cu-U: 5.0 ps AIMD at 700 K for $U_{\mathrm{eff}} = 6$ eV.

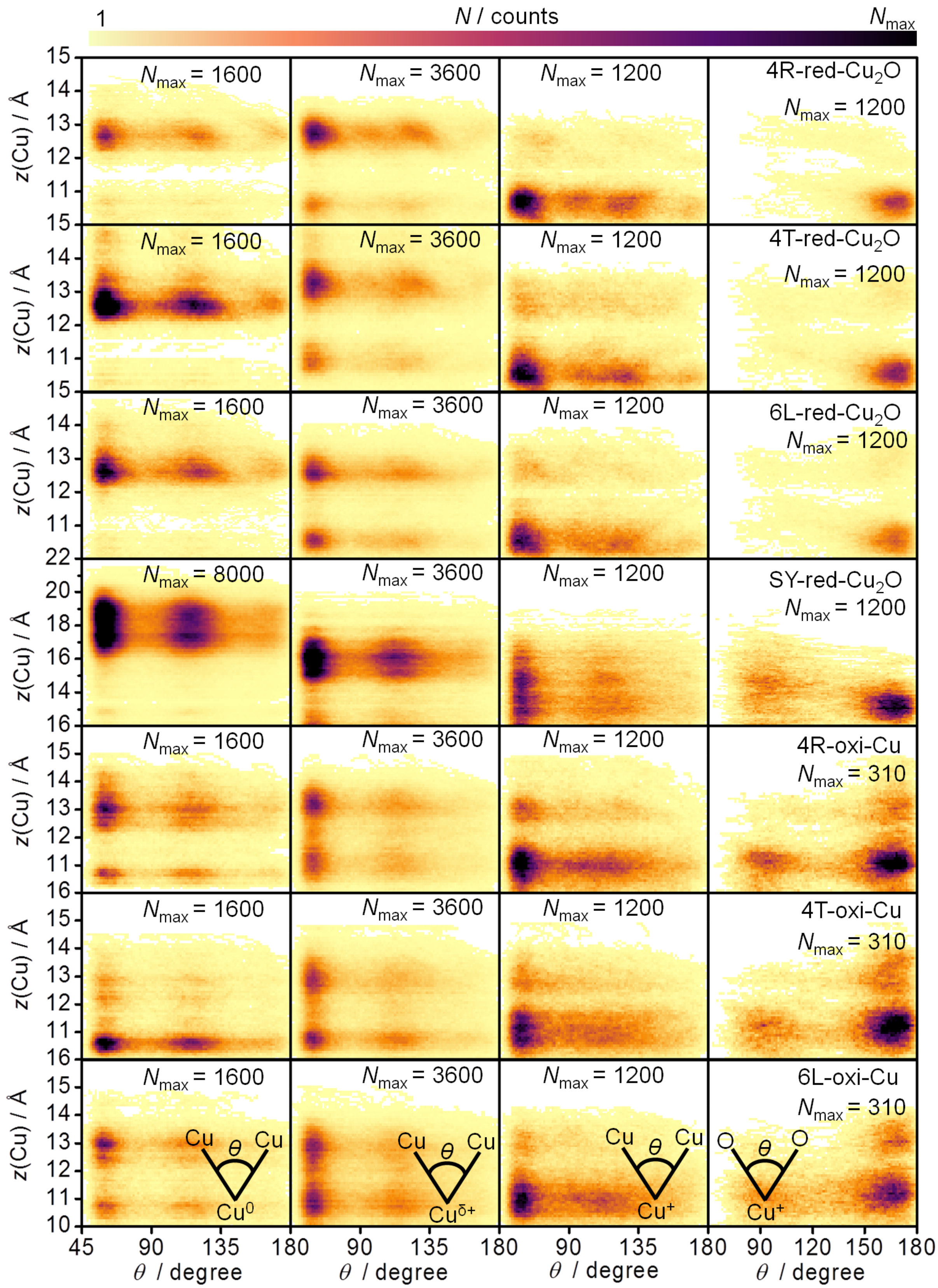

Figure S21: Histograms for angles $\theta(\mathrm{Cu}-\mathrm{Cu}^0-\mathrm{Cu})$, $\theta(\mathrm{Cu}-\mathrm{Cu}^{\delta+}-\mathrm{Cu})$, $\theta(\mathrm{Cu}-\mathrm{Cu}^{+}-\mathrm{Cu})$ and $\theta(\mathrm{O}-\mathrm{Cu}^{+}-\mathrm{O})$ at different heights $z(\mathrm{Cu})$.

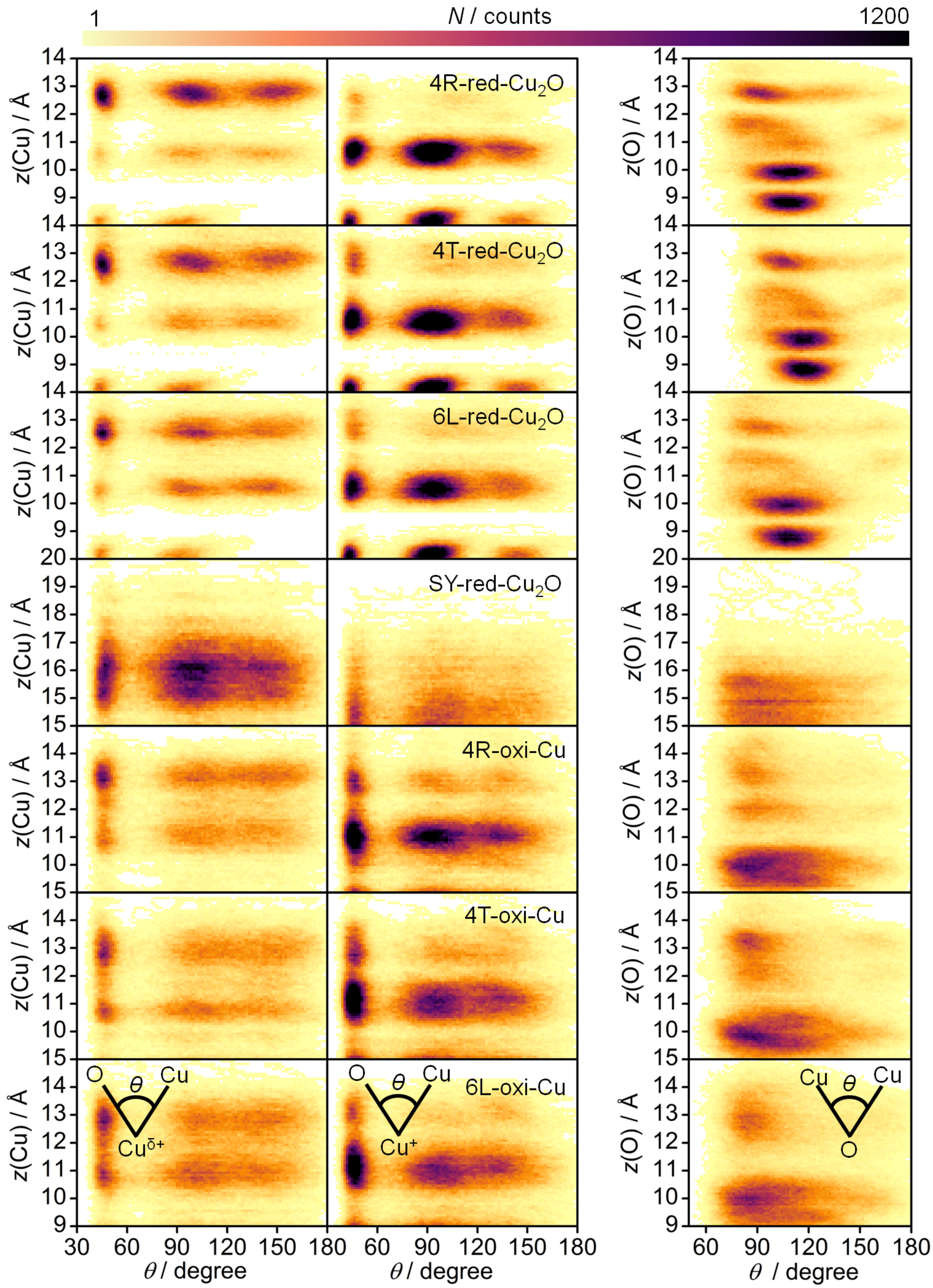

Figure S22: Histograms for angles $\theta(\mathrm{O}-\mathrm{Cu}^{\delta+}-\mathrm{Cu})$, $\theta(\mathrm{O}-\mathrm{Cu}^{+}-\mathrm{Cu})$ and $\theta(\mathrm{Cu}-\mathrm{O}-\mathrm{Cu})$ at different heights $z(\mathrm{Cu})$.

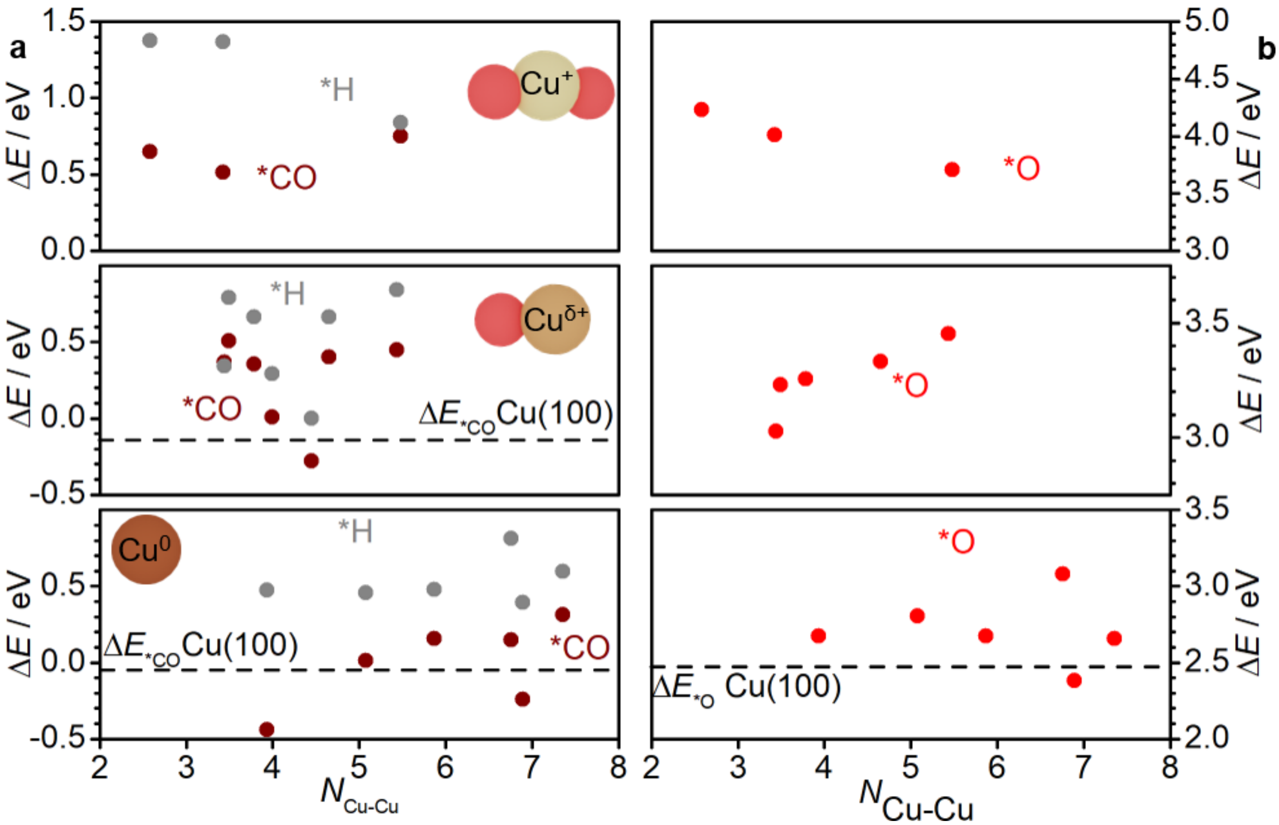

Figure S23: Adsorption energy of *CO, *H, and *O on Cu^0, $Cu^{\delta+}$, and Cu^+ as a function of coordination numbers. a, low coordinated metallic sites present stronger CO adsorption than Cu(100) surface sites (**Table S10**). $Cu^{\delta+}$ species range from highly endothermic *CO adsorption energies to strong tethering sites, depeding on its coordination. CO adsorption on Cu^+ sites is constant, $\Delta E_{*CO} > 0.5$ eV. For all the species, *H asorption is less favored than CO tethering. **b**, all the detected Cu species are less oxophilic than crystalline Cu, where oxophilicity is here parametrized as the energy to adsorb an oxygen atom atop. Metallic sites departs from Cu(100) behaviour at low coordination numbers. Both $Cu^{\delta+}$ and Cu^+ are even more oxophobic, given the saturation of their bonds by 1 and 2 oxygens atoms. In the future, local Cu coordination and oxophilicity may be applied to account for the wide product distribution of OD-Cu catalysts, **Table S1**.

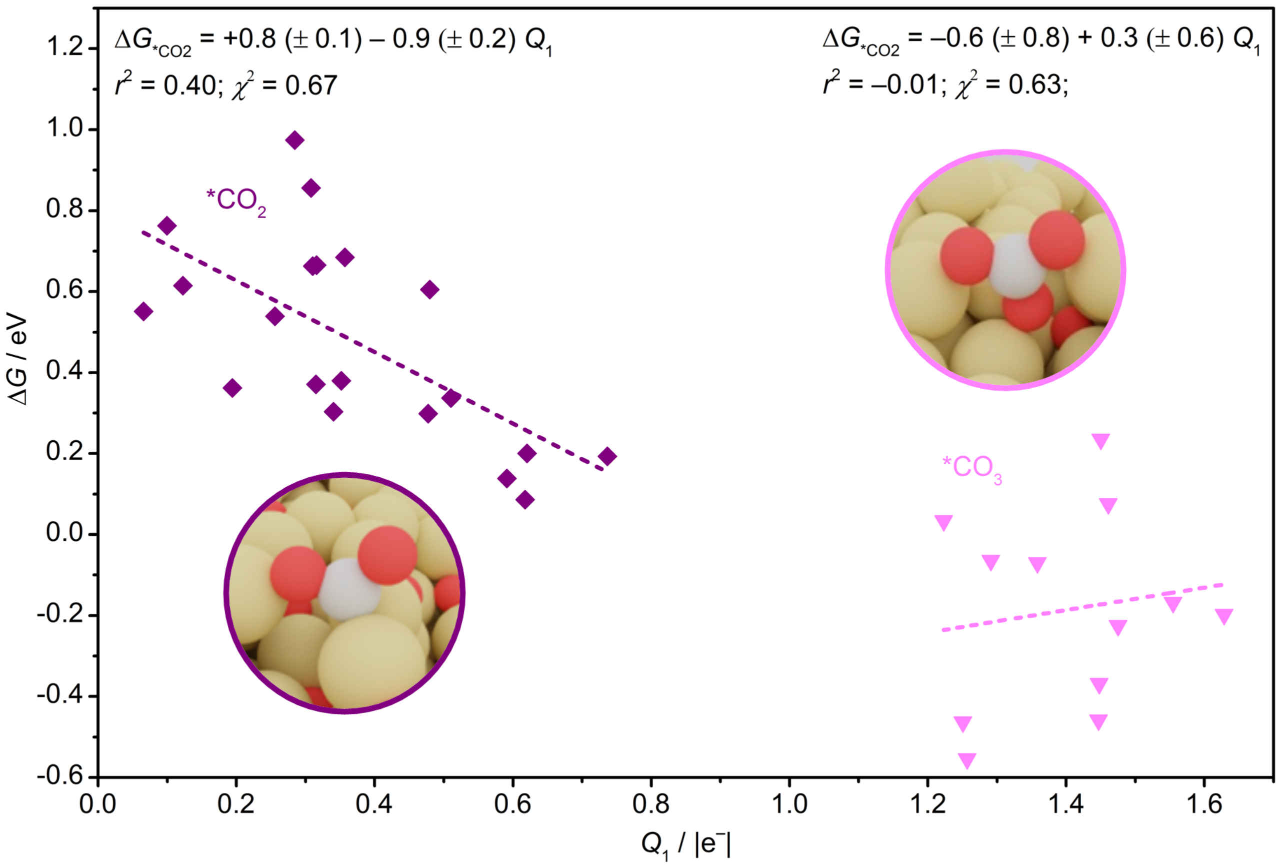

Figure S24: CO_2 binding energy vs ensemble polarization. We here reproduced **Figure 4a** by differentiating CO_2 adsorption on Cu site ($\eta^2_{\mathrm{C,O}}$, purple) and O site ($\eta^3_{\mathrm{O,C,O}}$, magenta). While CO_2 binding energy scales linearly with ensembles polarization on Cu sites, for the carbonate configuration CO_2 tethering saturates due to the high electronic density on the oxygen active site.

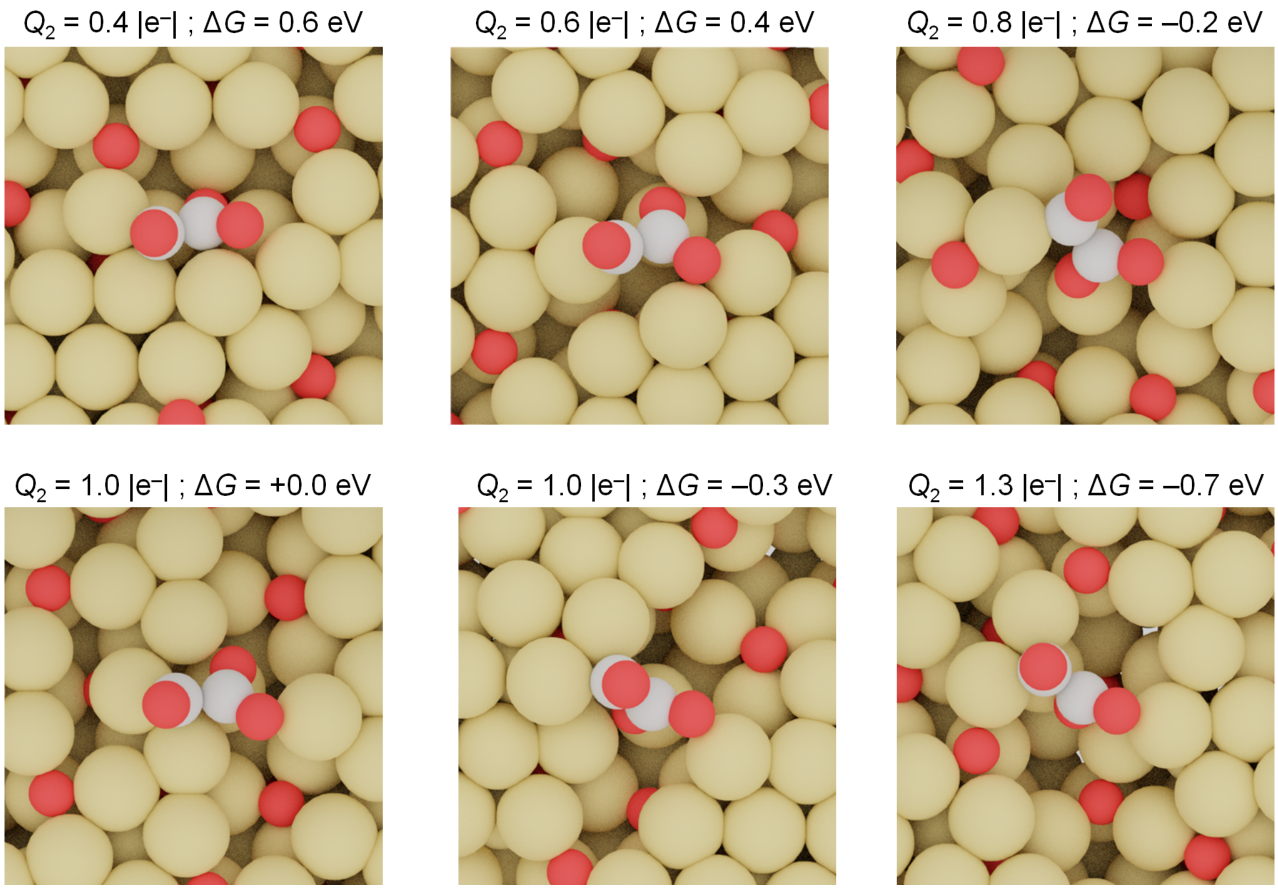

Figure S25: Local coordination of the glyoxylate-like configuration. We here report the local coordination of the six glyoxylate-like configurations inserted in **Figure 4b** together with the polarization of each ensemble and $\Delta G_{*\mathrm{OCCO}}$. Apart from a C-$O_{ns}$ bond, the glyoxylate intermediate is tethered to the surface with the second carbon atom on a bridge position or atop of low coordinated Cu^0 and $Cu^{\delta+}$ sites.

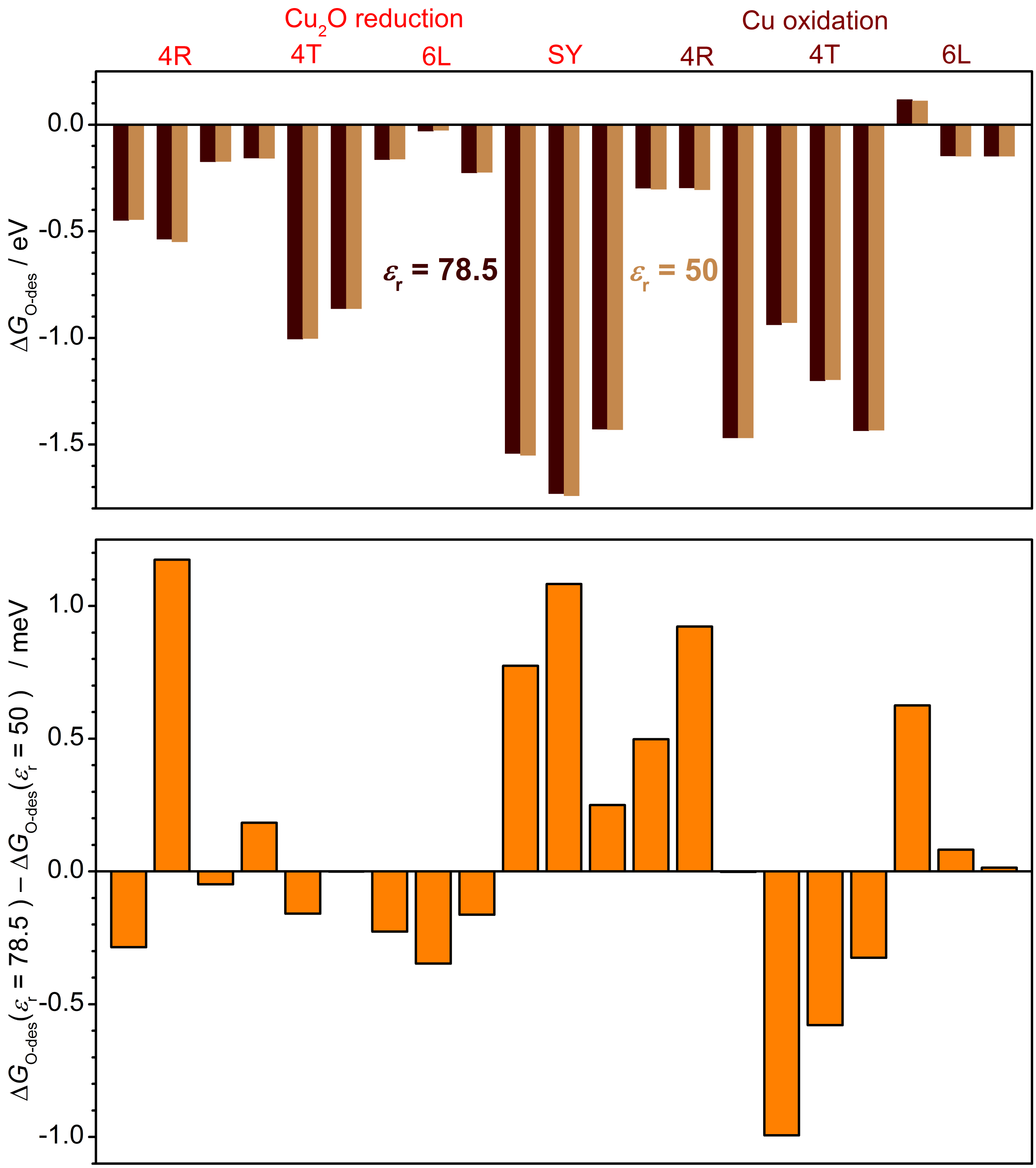

Figure S26: Dependence of dielectric permittivity on oxygen stability. Both initial and final configurations are less stabilized by the solvent at $\epsilon_r = 50.0$[82] (light colors) than $\epsilon_r = 78.5$ (dark colors). However, since solvation stabilizes both Cu_xO_y (top) and Cu_xO_{y-1} (down) almost equally, these contributions cancel each other, thus the stability of the sampled oxygen configurations is not affected by the dielectric permittivity of the solvent.

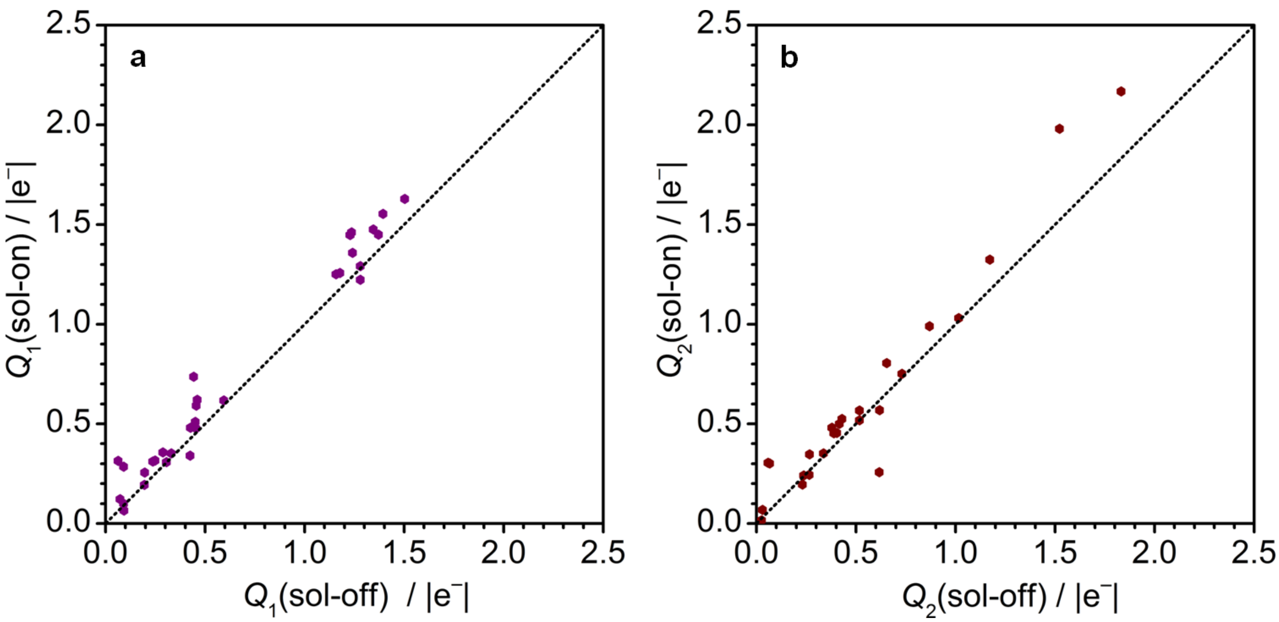

Figure S27: Uncertainty in the estimation of ensembles polarization. By applying implicit solvation, the Bader charges of the ensembles reported in **Figure 4a-b** change. In average **a**, Q_1 and **b**, Q_2 are 0.09 and 0.07 $|e^-|$ higher when solvation is included, thus the presence of the solvent does not significantly affect the linear correlation between C_{2+} intermediates binding energy and ensemble polarization, **Figure 4a-b**.

S4 Tables

Table S1: Previous experimental studies. U / V_{RHE}; observation: product (Faradaic efficiency). ERD-Cu: electro-redeposited Cu; Oxi-Cu: oxidized Cu; OD-Cu: oxide-derived Cu; PT: Plasma-treated; Lig-Cu: ligand-modified Cu; Cu GDE: Cu on Gas Diffusion Electrode configuration; NPs: nanoparticles; MOF: Metal-organic framework; NCs: nanocrystals; CV-Cu: cyclic voltammetry-treated Cu; LDH: layered double hydroxides; ED-Cu: electrodeposited Cu; NF: nanoflowers.

ref	Catalyst	U (V_{RHE})	Observation	Notes
78	ERD-Cu-CO_2	−0.70 V	C_{2+} (90%)	
88	CuO_x	−0.90 V	C_{2+} (80%)	Lithiation-controlled d_{atom}.
47	Oxi-Cu	−1.00 V	C_{2+} (76%)	
89	Au/Cu_2O	−0.50 V	C_{2+} (70%)	
90	CuO on Cu_3N	−0.95 V	C_{2+} (64%)	30h stability.
64	OD-Cu	−1.00 V	C_{2+} (60%)	Pre-oxidized Cu; O^{18} labelling.
91	OD-Cu	−0.40 V	C_{2+} (50%)	H_2-reduced Cu; CO Reduction.
92	Cu_2S	−0.95 V	C_{2+} (32%)	
93	PT Cu	−1.00 V	C_2 (69%)	
94	Cu-B	−1.10 V	C_2H_4 (80%)	
95	Cu_2O	−0.52 V	C_2H_4 (72%)	
96	Lig-Cu	−0.84 V	C_2H_4 (72%)	
97	Cu GDE	−0.65 V	C_2H_4 (70%)	
54	Cu/Cu_2O	−1.70 V	C_2H_4 (70%)	C_2H_4 from Cu^0/Cu^+.
56	PT Cu	−0.90 V	C_2H_4 (60%)	
98	Cu_2O NPs	−1.10 V	C_2H_4 (59%)	
99	CuBr	−1.10 V	C_2H_4 (51%)	Anodic halogenation.
100	OD-Cu	−1.00 V	C_2H_4 (50%)	
101	CuCl	−1.80 V	C_2H_4 (50%)	

ref	Catalyst	U / V_{RHE}	Observation	Notes
102	Cu_mCeO_x	−1.10 V	C_2H_4 (48%)	Cu_xO_y on a Ceria support.
52	Cu_4O	−1.00 V	C_2H_4 (45%)	Oxygen-Bearing Cu.
103	Cu on MOF	−1.07 V	C_2H_4 (45%)	
104	OD-Cu	−0.98 V	C_2H_4 (43%)	
105	Cu NCs	−1.10 V	C_2H_4 (41%)	
68	Cu(I)O	−0.99 V	C_2H_4 (40%)	
106	CV Cu	−1.00 V	C_2H_4 (40%)	
57	ERD-Cu	−1.20 V	C_2H_4 (40%)	
46	OD-Cu	−1.08 V	C_2H_4 (38%)	Anoxidized Cu, 40h stability.
107	Cu	−1.30 V	C_2H_4 (38%)	
108	Cu-Cu_2O LDH	−1.10 V	C_2H_4 (36%)	
109	OD-Cu	−0.98 V	C_2H_4 (32%)	
110	ED-Cu	−1.10 V	C_2H_4 (28%)	
49	ED-Cu_2O	−1.20 V	C_2H_4 (25%)	Suboxidic surface.
111	ED-Cu	−0.80 V	C_2H_4 (20%)	Surface oxidized Cu.
112	Cu	−1.10 V	C_2H_4 (20%)	
77	OD-Cu	−1.10 V	C_2H_4 (20%)	
113	OD-Cu/Ag	−1.10 V	C_2H_4 (15%)	
114	Cu/C	−0.70 V	C_2H_5OH (91%)	Cu single atom as active site.
115	NF Cu	−0.35 V	C_2H_5OH (60%)	CO reduction.
116	N-C/Cu	−0.68 V	C_2H_5OH (52%)	Electron donors favours ethanol.
84	OD-Cu NPs	−0.30 V	C_2H_5OH (45%)	
117	Cu-Ag	−0.67 V	C_2H_5OH (41%)	
118	Lig-Cu	−0.82 V	C_2H_5OH (41%)	Porphyrin-funtionalized Cu.
119	Cu-Ag	−1.20 V	C_2H_5OH (35%)	
120	N-Cu	−0.50 V	C_2H_5OH (29%)	Nitrogen-doped nanodiamonds/Cu.

ref	Catalyst	U / V_{RHE}	Observation	Notes
113	OD-Cu/Ag	−1.10 V	C_2H_5OH (18%)	
68	Cu(I)O	−0.99 V	C_2H_5OH (16%)	
99	CuI	−1.09 V	C_2H_5OH (14%)	Anodic halogenation.
121	Cu-Ag	−0.46 V	n-PrOH (33%)	
122	OD-Cu	−0.47 V	n-PrOH (23%)	
123	CuI	−0.45 V	n-PrOH (20%)	
124	ED-Cu	−0.95 V	n-PrOH (8%)	12h stability.
125	U-Cu	−0.83 V	n-PrOH (5%)	Urea-modified Cu foam.
107	Cu	−1.30 V	C_2H_6 (46%)	
111	ED-Cu	−0.60 V	C_2H_6 (37%)	Surface oxidized Cu.
120	N-Cu	−0.50 V	Acetate (35%)	Nitrogen-doped nanodiamonds/Cu.
126	PT Ag	−0.60 V	CO (90%)	
112	Cu NPs	−1.10 V	CO (25%)	
127	GO-Cu_xO	−0.80 V	HCOOH (81%)	Cu_xO-decorated graphene oxide.
112	Cu	−1.10 V	CH_4 (57%)	
106	CV Cu	−1.00 V	CH_4 (35%)	
106	ED-Cu	−1.00 V	CH_4 (30%).	Surface oxidized Cu.
112	Cu NPs	−1.10 V	H_2 (65%)	
106	ED-Cu	−1.00 V	H_2 (50%)	Surface oxidized Cu.
106	Cu	−1.00 V	H_2 (50%)	

Table S2: Summary of the outcomes of the present study.

Theoretical outcomes	Experimental evidences
Residual O stable until −0.84 V vs RHE due to the high surface pH at CO_2 reduction conditions, **Figure S4**.	• CuO Raman and Auger signals at −0.56 V vs RHE.[52] • High oxygen content for OD-Cu under reduction conditions by XPS and XANES.[46] • 20% Cu^{+} fraction after 2h at −0.95 vs RHE.[53] • Cu_2O Auger signals on Cu(100) under pulsed electrolysis.[47] • Cu-O EXAFS signal after electrochemical reduction.[54] • Subsurface O in Cu foil and nanoparticles after oxidation-reduction cycles.[45,51]

Theoretical outcomes	Experimental evidences
High surface area for red-Cu_2O and oxi-Cu models: atomic surface roughness between 0.8-1.4 Å, **Figure S9**.	• Crystalline Cu atomic surface roughness: 0.32 Å.[128] • Roughness factor of 26.4 for O_2-treated Cu (1 for pristine Cu).[56] • Roughness factor of 1.1 for Cu(100) under pulsed electrolysis.[47]
Oxygen-depleted regions detected by simulated STM images, **Figure S3**.	• Dark and light areas on a Cu_2O/Cu system after CO autocatalytic reduction, respectively oxygen-depleted and oxidic regions.[85]
Three states for Cu depending on coordination to O: metallic Cu^0 (0 O), polarized $Cu^{\delta+}$ (1 O) and oxidic Cu^+ (2 O), **Figure 2**.	• Suboxidic Cu detected *via* Auger spectroscopy[44] and *via in situ* FT-EXAFS until −1.0 V vs RHE.[52] Average Cu-O coordination number of 1.1 *via* EXAFS.[52] • Cu^+ species under reduction conditions.[47,53] 23% Cu^+ detected *via* XAS at −1.2 V vs RHE.[57]

Theoretical outcomes	Experimental evidences
Three well-defined states for oxygen depending on its coordination to neighboring Cu atoms: either 3, 4 and 5, **Figure 3**.	• No experimental reports of O coordination on OD-Cu available yet.
14 structural ensembles, **Figure 3g** which do not depend on AIMD temperatures, **Figures S18-S19**, or Hubbard parameter, **Figure S20**. Among them, low coordinated copper adatoms, crystalline facets, $Cu_3^+O_3$.	• Average Cu-Cu coordination number on OD-Cu of 6.6, 3.08, 1.84 through EXAFS.[52,114] • Cu(100) for air-oxidized Cu upon reconstruction under reduction conditions.[61,71] • Similar structural fingerprints between experimentally detected Cu_4O (ref 52) and $Cu_3^+O_3$.
CO_2 reduction activity correlates positively with ensembles polarizability of the ensembles, **Figure 4a**.	• Adsorbed CO_2^- detected *via* SEIRAS from −0.4 V vs RHE on Cu^0, from −0.2 V vs RHE mixed Cu^0/Cu^+ sites and from −0.1 V vs RHE on Cu^+.[106] • Selectivity toward Hydrogen Evolution Reduction decreases at high anodization time.[47]

Theoretical outcomes	Experimental evidences
Near-surface oxygen promotes C-C coupling *via* a glyoxylate-like configuration, **Figure 4b**.	• Experimental vibrational frequencies for CO_2 reduction reactants (**Table S11**) compatible with glyoxylate-like configuration (**Table S14**): $\nu_{\text{glyoxylate-1}} = 1630$ cm^{-1} (CO_{hollow}: 1677 cm^{-1}, ref 129), $\nu_{\text{glyoxylate-2}} = 1479$ cm^{-1} (CO_3^{2-}: 1510 cm^{-1}, ref 129), and $\nu_{\text{glyoxylate-3}} = 1145$ cm^{-1} (hydrogenated dimer: 1191 cm^{-1}, ref 130).
CO-CO adsorption *via* a glyoxylate-like configuration promotes ethanol, **Figure 4b**.	• Ethanol selectivity increases at high anodization times and high surface polarization.[47] • CO reduction to ethylene does not correlate with average Cu oxidation state measured *via Operando* XANES.[131]

Table S3: Copper oxide formation energies by Cu atom for pristine and reconstructed OD-Cu models. Oxygen atomic percentage, $\frac{N_{\mathbf{O}}}{N_{\mathbf{Cu}}+N_{\mathbf{O}}} \cdot 100$, and copper-oxide formation energy per Cu atom, $E_{\mathbf{Cu_2O}}\ N_{\mathbf{Cu}}^{-1}$ / eV, for the modeled systems. Trajectories at $t = 0$ ps correspond to the pristine structures relaxed before equilibration, whilst trajectories at $t = 11$ ps stand for final structures relaxed after ab initio molecular dynamics. Red (ox) subscript labels Cu_2O (Cu oxidation) reduction models.

System	N_{Cu}	N_O	O %	$E_{Cu_2O}\ N_{Cu}^{-1}$ (0 ps) / eV	$E_{Cu_2O}\ N_{Cu}^{-1}$ (10 ps) / eV
$4R_{red}$	288	128	31	0.60	0.60
$4T_{red}$	288	128	31	0.59	0.60
$6L_{red}$	288	126	30	0.60	0.59
SY_{ox}	336	48	13	0.35	0.34
$4R_{ox}$	444	56	11	0.21	0.18
$4T_{ox}$	444	56	11	0.21	0.18
$6L_{ox}$	444	54	11	0.22	0.18

Table S4: Configurational entropy for OD-models. ΔS has been calculated according to Equations S5-S7. $T = 298.15$ K, room temperature. $T \cdot (\Delta S_{n=100} - \Delta S_{n=10}) < 0.01$ eV.

					$-T \cdot \Delta S(n \cdot 2\sqrt{3} \times n \cdot 2\sqrt{3})$ / eV		
System	N_{Cu}	$N_{O\text{-res}}$	$N_{O\text{-max}}$	N layers	$n = 1$	$n = 10$	$n = 100$
$4R_{red}$	192	80	96	4	−1.02	−1.08	−1.08
$4T_{red}$	192	80	96	4	−1.02	−1.08	−1.08
$6L_{red}$	192	78	96	4	−1.10	−1.15	−1.15
SY_{red}	336	48	168	7	−2.44	−2.50	−2.50
$4R_{ox}$	294	56	147	6	−2.37	−2.43	−2.43
$4T_{ox}$	294	56	147	6	−2.37	−2.43	−2.43
$6L_{ox}$	294	54	147	6	−2.34	−2.41	−2.41

Table S5: DFT energy, solvation energy and configurational entropy for the modeled systems. $-T{\cdot}\Delta S$ is calculated in Table S4. Red (ox) subscript labels Cu_2O reduction (Cu oxidation).

Surfaces	N_{Cu}	N_O	E / eV	ΔE_{sol} / eV	$-T{\cdot}\Delta S$ / eV
Cu_2O	2	1	−13.34	−0.02	–
Cu	1	0	−3.56	−0.01	–
$4R_{red}$	288	128	−1807.73	−2.60	−1.08
$4T_{red}$	288	128	−1807.23	−3.08	−1.08
$6L_{red}$	288	126	−1795.28	−2.70	−1.15
SY_{ox}	336	48	−1439.02	−0.82	−2.50
$4R_{ox}$	444	56	−1916.49	−1.61	−2.43
$4T_{ox}$	444	56	−1918.68	−1.52	−2.43
$6L_{ox}$	444	54	−1903.27	−1.26	−2.41

Table S6: Formation energies for OD-Cu models. Calculated for copper oxidation: Cu → Cu_xO_y (Equation S8), or Cu_2O reduction: Cu_xO_y → Cu_2O (Equation S9). Red (ox) subscript labels Cu_2O reduction (Cu oxidation). ΔG represents suboxide formation energy with respect to Cu_2O, $G_{Cu_xO_y} - G_{Cu_2O}$.

Surfaces	N_{Cu} (x)	N_O (y)	Cu → Cu_xO_y / eV	Cu_xO_y → Cu_2O / eV	ΔG / eV
Cu_2O	2	1	0.60	0.60	–
Cu	1	0	–	–	–
$4R_{red}$	288	128	0.67	0.17	0.07
$4T_{red}$	288	128	0.67	0.16	0.07
$6L_{red}$	288	126	0.66	0.25	0.05
SY_{red}	336	48	1.17	0.38	0.57
$4R_{ox}$	444	56	0.70	0.57	0.10
$4T_{ox}$	444	56	0.69	0.58	0.08
$6L_{ox}$	444	54	0.72	0.57	0.11

Table S7: Formation energies for metastable copper oxides. Calculated for copper oxidation: Cu → Cu_xO_y (Equation S8), or Cu_2O reduction: Cu_xO_y → Cu_2O (Equation S9). Cu_8O and $Cu_{64}O$ bulk structures were obtained from experimental characterization.[31,32] ΔG represents suboxide formation energy with respect to Cu_2O, $G_{Cu_xO_y} - G_{Cu_2O}$.

Bulk	N_{Cu} (x)	N_O (y)	E / eV	Cu → Cu_xO_y / eV	Cu_xO_y → Cu_2O / eV	ΔG / eV
Cu_2O	4	2	−27.20	0.64	0.64	–
Cu	1	0	−3.72	–	–	–
Cu_8O	16	2	−70.07	1.08	0.50	0.43
$Cu_{64}O$	128	2	−484.67	1.50	0.61	0.83

Table S8: Average Cu coordination numbers for Cu^0, $Cu^{\delta+}$, and Cu^+ species. Values reported as $\overline{x} \pm 3\sigma$ and calculated from coordination number distribution over time, Figure S14, after a stabilization period of $\Delta t = 6$ ps.

	Cu^0	$Cu^{\delta+}$	Cu^+
$\overline{N}_{\text{Cu-fcc}}$	12	–	–
$\overline{N}_{\text{Cu(111)}}$	9	–	–
$\overline{N}_{\text{Cu(100)}}$	8	–	–
$\overline{N}_{\text{Cu(110)}}$	7	–	–
$\overline{N}_{\text{4R-red}}$	4.9 ± 1.1	3.6 ± 0.5	2.0 ± 0.6
$\overline{N}_{\text{4T-red}}$	5.2 ± 0.7	3.8 ± 0.6	2.0 ± 0.6
$\overline{N}_{\text{6L-red}}$	5.0 ± 0.7	4.1 ± 0.5	2.1 ± 0.6
$\overline{N}_{\text{SY-red}}$	6.0 ± 0.4	5.0 ± 0.6	2.7 ± 0.2
$\overline{N}_{\text{4R-ox}}$	5.9 ± 1.4	4.5 ± 0.5	2.6 ± 0.5
$\overline{N}_{\text{4T-ox}}$	6.7 ± 1.3	4.7 ± 0.7	2.3 ± 0.6
$\overline{N}_{\text{6L-ox}}$	5.8 ± 1.4	4.5 ± 0.5	2.6 ± 0.6

Table S9: Relative abundance for Cu^0, $Cu^{\delta+}$, and Cu^+ species. Values are reported as $\overline{x} \pm 3\sigma$ of the relative abundances over time, Figure S16 after a stabilization period of $\Delta t = 6$ ps. Oxygen atomic percentage: $\frac{N_O}{N_{Cu}+N_O}$.

System	Cu^0 / %	$Cu^{\delta+}$ / %	Cu^+ / %	O %
$4R_{red}$	11 ± 4	43 ± 6	45 ± 4	31
$4T_{red}$	16 ± 4	37 ± 5	47 ± 4	31
$6L_{red}$	18 ± 8	44 ± 14	38 ± 8	30
SY_{red}	55 ± 3	29 ± 4	16 ± 3	13
$4R_{ox}$	14 ± 6	62 ± 9	23 ± 9	11
$4T_{ox}$	17 ± 10	61 ± 13	22 ± 10	11
$6L_{ox}$	12 ± 11	69 ± 15	19 ± 13	11

Table S10: Adsorption energies of relevant intermediates on Cu single crystal. ΔG: DFT adsorption energies for CO_2, CO and H on crystalline Cu at 0.0 V vs. RHE, in eV, as calculated in our previous work.[132]

ΔG / eV	Cu(100)	Cu(111)	Cu(110)	Cu(211)
$*CO_2$	+0.71	+0.73	+0.96	+1.24
*CO	−0.46	−0.17	−0.03	−0.25
*H	−0.12	−0.14	−0.06	−0.03

Table S11: Experimental vibrational frequencies for C_{2+} intermediates on Cu.

ref	ν_1 / cm^{-1}	Assignment
133	2080-2040	CO
129	2070-2058	CO
134	1720	CHO
130	1677	CO (hollow site)
130	1600	H_2O
130	1584	*OCCOH
134	1544-1517	$*CO_3^{2-}$
129	1510	$*CO_3^{2-}$ ($U = +0.4$ V vs RHE)
129	1429	$*CO_3^{2-}$ ($U = -0.3$ V vs RHE)
130	1191	*OCCOH

Table S12: CO_2 generation from adsorbed CO. If oxygen adsorption sites tether CO too strongly, OCCO dimerization step is hindered by the desorption of surface oxygen as a CO_2 molecule, $CO + Cu_xCu_y \rightarrow CO_2 + Cu_xO_{y-1}; \Delta G_{CO_2\text{-des}}$.

Configuration	$\Delta G_{CO_2\text{-des}}$ / eV
O-1	−0.18
O-2	−0.33
O-3	−0.44
O-4	−0.44
O-5	−0.45
O-6	−0.46
O-7	−0.47
O-8	−0.52
O-9	−0.59
O-10	−0.59
O-11	−0.74
O-12	−0.83
O-13	−1.16
O-14	−1.23
O-15	−1.30
O-16	−1.50
O-17	−1.72
O-18	−1.73
O-19	−1.76
O-20	−1.84
O-21	−2.03

Table S13: Glyoxylate and oxalate formation energies. Glyoxylate-like, $OCCO_2^-$ and oxalate intermediates can be formed prior to CO formation from direct CO_2 on strong tethering sites: $2* + 2CO_2 + 2H^+ + 3e^- \rightarrow OC{*}CO_2^- + H_2O$, $\Delta E_{OC*CO_2^-}$; $2* + 2CO_2 + 2e^- \rightarrow C_2O{*}_4^{2-}$, $\Delta E_{C_2O_4^{2-}}$. Gly-n: glyoxylate-like intermediate; Oxa-n: oxalate. Energy references: $E_{H_2O} = -14.22$ eV; $E_{H_2} = -6.77$ eV; $E_{CO_2} = -22.96$ eV.

Intermediate	ΔE_{*X} / eV
Gly-1	−0.47
Gly-2	−0.25
Gly-3	+1.29
Gly-4	+0.46
Gly-5	−0.46
Gly-6	−0.28
Oxa-1	−0.41
Oxa-2	−0.42

Table S14: DFT vibrational frequencies for glyoxylate-like and oxalate intermediates adsorbed on red-Cu_2O surfaces. The highest vibrational modes, ν_i, are reported for the new intermediates to allow comparison with infrared spectroscopy characterization. $\overline{\nu_i}$ represents the average of the vibrational modes related to the same configuration; $\Delta\nu_i$ is calculated as $3\sigma_{\nu_i}$ if more than three values n were available, $\frac{\max_{\nu_i}-\min_{\nu_i}}{2}$ if $n \leq 3$.

	glyoxylate-like			oxalate		
n	ν_1 / cm^{-1}	ν_2 / cm^{-1}	ν_3 / cm^{-1}	ν_1 / cm^{-1}	ν_2 / cm^{-1}	ν_3 / cm^{-1}
#1	1634	1553	1200	1727	1710	1176
#2	1623	1497	1126	1473	1430	1251
#3	1553	1366	945	–	–	–
#4	1698	1380	1163	–	–	–
#5	1673	1533	1271	–	–	–
#6	1602	1546	1167	–	–	–
$\overline{\nu_i}$	1630	1479	1145	1600	1570	1213
$\Delta\nu_i$	155	254	329	127	140	37

Table S15: DFT vibrational frequencies for adsorbed carbonate and COCO dimer. The highest vibrational modes, ν_i, are reported for adsorbed carbonate and OCCO dimer, either adsorbed as *OCCO or OC*C*O on Cu atom. $\overline{\nu_i}$ represents the average of the vibrational modes; $\Delta\nu_i$ is calculated as $3\sigma_{\nu_i}$ if more than three values n were available, $\frac{\max_{\nu_i}-\min_{\nu_i}}{2}$ if $n \leq 3$. The dehydrogenated OCCO dimer presents similar fingerprints as hydrogenated OCCO dimer adsorbed on Cu(100), see Table S11.

	$^*CO_3^{2-}$		*OCCO		OC*C*O	
n	ν_1 / cm^{-1}	ν_2 / cm^{-1}	ν_1 / cm^{-1}	ν_2 / cm^{-1}	ν_1 / cm^{-1}	ν_2 / cm^{-1}
#1	1615	1262	2037	1210	1710	1601
#2	1601	1227	1995	1223	1727	1696
#3	1564	1276	2033	1172	1669	1428
#4	1625	1233	2027	1210	–	–
#5	1511	1226	1968	1344	–	–
#6	1708	1060	1983	1366	–	–
#7	1488	1259	1996	1244	–	–
#8	1630	1246	1994	1119	–	–
#9	1546	1226	1973	1343	–	–
#10	1595	1216	1998	1231	–	–
#11	1542	1222	–	–	–	–
#12	1630	1235	–	–	–	–
$\overline{\nu_i}$	1588	1224	2000	1246	1702	1575
$\Delta\nu_i$	182	165	73	242	29	134

Table S16: Dipole moments for *OCCO, glyoxylate, and oxalate and stabilization due to applied potential. (surf) and (surf + ads) correspond to the z-projection of the electric dipole moment of the clean surface and surface plus adsorbed molecules. The net electric dipole moment is calculated as p_z(net) = p_z(surf+ads) − p_z(surf). An applied negative electric potential (here −1.0 V vs RHE) stabilizes the negative intermediates. We calculated the contribution to the adsorption energies following the computational hydrogen electrode approach[22] and assuming a potential of zero charge of the surfaces of −0.73 V vs SHE (polycrystalline Cu at neutral pH, ref 135). The applied potential stabilizes all the intermediates equally, since each of them forms from 2*CO through a single electron transfer. TS = Transition State.

Electric dipole moment / eÅ	*OCCO Cu(100)	*OCCO	glyoxylate-like	oxalate
2*CO (surf)	< 0.01	+0.84	+0.71	+1.75
TS (surf) /	−0.01	+0.79	+0.88	+1.06
$*C_2O_2$ (surf)	−0.01	+0.78	+0.88	+1.14
2*CO (surf + ads)	+0.23	+0.81	+1.08	+0.80
TS (surf + ads)	+0.18	+1.08	+1.15	+1.41
$*C_2O_2$ (surf + ads)	+0.25	+1.41	+1.17	+0.82
2*CO (net)	+0.23	−0.03	+0.37	−0.95
TS (net)	+0.19	+0.29	+0.27	+0.35
$*C_2O_2$ (net)	+0.26	+0.63	+0.28	−0.32
ΔG Stabilization / eV				
2*CO	−0.05	+0.01	−0.08	+0.22
TS	−0.04	−0.07	−0.06	−0.08
$*C_2O_2$	−0.06	−0.14	−0.06	+0.07

Table S17: Regression parameters between CO_2 activity (C_{2+} selectivity) and ensembles polarization. $\Delta G_{*CO_2^-}$ vs Q_1, ΔG_{2*CO} vs Q_2 and ΔG_{*OCCO^-} vs Q_2, $\Delta G_{*X} = a + b \cdot Q_i$.

ΔG_{*X}	a / eV	b / V	r^2	χ^2
$* + CO_2 + e^- \rightarrow *CO_2^-$	+0.7 ± 0.1	−0.6 ± 0.1	0.70	1.49
$2* + 2CO_2 + 4H^+ + 4e^- \rightarrow 2*CO + 2H_2O$	−1.3 ± 0.1	+1.3 ± 0.1	0.83	2.18
$2* + 2CO_2 + 4H^+ + 5e^- \rightarrow *OCCO^- + 2H_2O$	+0.7 ± 0.1	−0.7 ± 0.1	0.66	1.63

Table S18: Copper oxide formation energies for different Hubbard corrections. Copper oxide formation energies, $E_{\mathbf{Cu_2O}}$, were computed from DFT energies according to Equation S2. Solvation and entropy were included through experimental corrections.[26] Both theoretical and experimental formation energies are reported vs. H_2O. $U_{\text{eff}} = U - J$, with $J = 1$ eV.

	$E_{\mathrm{Cu_2O}}$		$G_{\mathrm{Cu_2O}}$	
	11 e^-	17 e^-	11 e^-	17 e^-
Exp.[26]	1.21	–	0.94	–
DFT	1.31	1.29	0.96	0.94
$U_{\text{eff}} = 0$	1.26	1.26	0.90	0.91
$U_{\text{eff}} = 1$	1.20	1.19	0.84	0.84
$U_{\text{eff}} = 2$	1.13	1.13	0.78	0.77
$U_{\text{eff}} = 3$	1.07	1.07	0.72	0.71
$U_{\text{eff}} = 4$	1.01	1.01	0.66	0.66
$U_{\text{eff}} = 5$	0.96	0.96	0.60	0.61
$U_{\text{eff}} = 6$	0.90	0.91	0.54	0.56

Table S19: Energetic convergence for different k-points sampling. The energy for a surface-CO_2 intermediate system with a different Γ-centered k-points meshes from the Monkhorst-Pack method (ref 5) was obtained. All energies were equivalent within Density Functional Theory accuracy, $\Delta E = 0.01$ eV. Therefore, for all the simulations we sampled the Brillouin zone only with the Γ-point.

k-points	E / eV	ΔE / eV
1×1×1	−1830.00	
2×2×1	−1830.01	0.01
3×3×1	−1830.01	< 0.01
4×4×1	−1830.02	< 0.01

Table S20: Effect of Hubbard correction on the ensembles thermochemical properties. We calculated the adsorption energies of a common reaction intermediate, CO_2, varying U_{eff}. The energies were equivalent within $\Delta E = 0.12$ eV.

Functional	ΔE / eV
PBE	−0.45
PBE + U ($U_{\text{eff}} = 3.0$ eV)	−0.42
PBE + U ($U_{\text{eff}} = 6.0$ eV)	−0.33

Supporting References

(1) Kresse, G.; Furthmüller, J. Efficiency of ab-initio total energy calculations for metals and semiconductors using a plane-wave basis set. *Computat. Mater. Sci.* **1996**, *6*, 15–50.

(2) Kresse, G.; Furthmüller, J. Efficient iterative schemes for ab initio total-energy calculations using a plane-wave basis set. *Phys. Rev. B* **1996**, *54*, 11169–11186.

(3) Perdew, J. P.; Burke, K.; Ernzerhof, M. Generalized gradient approximation made simple. *Phys. Rev. Lett.* **1996**, *77*, 3865–3868.

(4) Blöchl, P. E. Projector augmented-wave method. *Phys. Rev. B* **1994**, *50*, 17953–17979.

(5) Monkhorst, H. J.; Pack, J. D. Special points for Brillouin-zone integrations. *Phys. Rev. B* **1976**, *13*, 5188–5192.

(6) Dudarev, S. L.; Botton, G. A.; Savrasov, S. Y.; Humphreys, C. J.; Sutton, A. P. Electron-energy-loss spectra and the structural stability of nickel oxide: An LSDA+U study. *Phys. Rev. B* **1998**, *57*, 1505–1509.

(7) Isseroff, L. Y.; Carter, E. A. Importance of reference Hamiltonians containing exact exchange for accurate one-shot GW calculations of Cu_2O. *Phys. Rev. B* **2012**, *85*, 235142.

(8) Bendavid, L. I.; Carter, E. A. First-principles predictions of the structure, stability, and photocatalytic potential of Cu_2O surfaces. *J. Phys. Chem. B* **2013**, *117*, 15750–15760.

(9) Heinemann, M.; Eifert, B.; Heiliger, C. Band structure and phase stability of the copper oxides Cu_2O, CuO, and Cu_4O_3. *Phys. Rev. B* **2013**, *87*, 115111.

(10) Ikuno, T.; Zheng, J.; Vjunov, A.; Sanchez-Sanchez, M.; Ortuño, M. A.; Pahls, D. R.; Fulton, J. L.; Camaioni, D. M.; Li, Z.; Ray, D. et al. Methane oxidation to methanol catalyzed by Cu-Oxo clusters stabilized in NU-1000 metal-organic framework. *J. Am. Chem. Soc.* **2017**, *139*, 10294–10301.

(11) Vogiatzis, K. D.; Li, G.; Hensen, E. J.; Gagliardi, L.; Pidko, E. A. Electronic structure of the $[Cu_3(\mu\text{-}O)_3]^{2+}$ cluster in mordenite zeolite and its effects on the methane to methanol oxidation. *J. Phys. Chem. B* **2017**, *121*, 22295–22302.

(12) Marx, D.; Hutter, J. *Ab initio molecular dynamics: basic theory and advanced methods*; Cambridge University Press, 2009.

(13) Nosé, S. A unified formulation of the constant temperature molecular dynamics methods. *J. Chem. Phys.* **1984**, *81*, 511–519.

(14) Hoover, W. G. Canonical dynamics: Equilibrium phase-space distributions. *Phys. Rev. A* **1985**, *31*, 1695–1697.

(15) Grimme, S. Semiempirical GGA-type density functional constructed with a long-range dispersion correction. *J. Comput. Chem.* **2006**, *27*, 1787–1799.

(16) Bučko, T.; Hafner, J.; Lebegue, S.; Angyán, J. G. Improved description of the structure of molecular and layered crystals: ab initio DFT calculations with van der Waals corrections. *J. Phys. Chem. A* **2010**, *114*, 11814–11824.

(17) Almora-Barrios, N.; Carchini, G.; Błoński, P.; López, N. Costless derivation of dispersion coefficients for metal surfaces. *J. Chem. Theory Comput.* **2014**, *10*, 5002–5009.

(18) Fishman, M.; Zhuang, H. L.; Mathew, K.; Dirschka, W.; Hennig, R. G. Accuracy of exchange-correlation functionals and effect of solvation on the surface energy of copper. *Phys. Rev. B* **2013**, *87*, 245402.

(19) Mathew, K.; Sundararaman, R.; Letchworth-Weaver, K.; Arias, T. A.; Hennig, R. G. Implicit solvation model for density-functional study of nanocrystal surfaces and reaction pathways. *J. Chem. Phys.* **2014**, *140*, 084106.

(20) Makov, G.; Payne, M. C. Periodic boundary conditions in ab initio calculations. *Phys. Rev. B* **1995**, *51*, 4014–4022.

(21) Peterson, A. A.; Abild-Pedersen, F.; Studt, F.; Rossmeisl, J.; Nørskov, J. K. How copper catalyzes the electroreduction of carbon dioxide into hydrocarbon fuels. *Energy Environ. Sci.* **2010**, *3*, 1311–1315.

(22) Nørskov, J. K.; Rossmeisl, J.; Logadottir, A.; Lindqvist, L.; Kitchin, J. R.; Bligaard, T.; Jónsson, H. Origin of the overpotential for oxygen reduction at a fuel-cell cathode. *J. Phys. Chem. B* **2004**, *108*, 17886–17892.

(23) Daelman, N.; Hegner, F. S.; Rellán-Piñeiro, M.; Capdevila-Cortada, M.; García-Muelas, R.; López, N. Quasi-degenerate states and their dynamics in oxygen deficient reducible metal oxides. *J. Chem. Phys.* **2020**, *152*, 050901.

(24) Gattinoni, C.; Michaelides, A. Atomistic details of oxide surfaces and surface oxidation: the example of copper and its oxides. *Surf. Sci. Rep.* **2015**, *70*, 424–447.

(25) Nie, X.; Griffin, G. L.; Janik, M. J.; Asthagiri, A. Surface phases of $Cu_2O(111)$ under CO_2 electrochemical reduction conditions. *Catal. Commun.* **2014**, *52*, 88–91.

(26) Lide, D. R. Handbook of Chemistry and Physics, 84^{th} edition. 2003.

(27) Rost, C. M.; Sachet, E.; Borman, T.; Moballegh, A.; Dickey, E. C.; Hou, D.; Jones, J. L.; Curtarolo, S.; Maria, J.-P. Entropy-stabilized oxides. *Nat. Commun.* **2015**, *6*, 8485.

(28) McQuarrie, D. A.; Simon, J. D. *Molecular thermodynamics*; 1999.

(29) Capdevila-Cortada, M.; López, N. Entropic contributions enhance polarity compensation for $CeO_2(100)$ surfaces. *Nat. Mater.* **2017**, *16*, 328–334.

(30) Hochella, M. F. J.; Carim, A. H. A reassessment of electron escape depths in silicon and thermally grown silicon dioxide thin films. *Surf. Sci.* **1988**, *197*, L260–L268.

(31) Guan, R.; Hashimoto, H.; Kuo, K. H. Electron-microscopic study of the structure of metastable oxides formed in the initial stage of copper oxidation. II. Cu_8O. *Acta Crystallogr., Sect B: Struct. Sci.* **1984**, *B40*, 560–566.

(32) Guan, R.; Hashimoto, H.; Kuo, K. H. Electron-microscopic study of the structure of metastable oxides formed in the initial stage of copper oxidation. III. $Cu_{64}O$. *Acta Crystallogr., Sect B: Struct. Sci.* **1985**, *B41*, 219–225.

(33) Persson, K. A.; Waldwick, B.; Lazic, P.; Ceder, G. Prediction of solid-aqueous equilibria: Scheme to combine first-principles calculations of solids with experimental aqueous states. *Phys. Rev. B* **2012**, *85*, 1–12.

(34) Singh, A. K.; Zhou, L.; Shinde, A.; Suram, S. K.; Montoya, J. H.; Winston, D.; Gregoire, J. M.; Persson, K. A. Electrochemical stability of metastable materials. *Chem. Mater.* **2017**, *29*, 10159–10167.

(35) Birgersson, M.; Almbladh, C. O.; Borg, M.; Andersen, J. N. Density-functional theory applied to Rh(111) and CO/Rh(111) systems: Geometries, energies, and chemical shifts. *Phys. Rev. B* **2003**, *67*, 045402.

(36) Köhler, L.; Kresse, G. Density functional study of CO on Rh(111). *Phys. Rev. B* **2004**, *70*, 165405.

(37) Garofalini, S. H. Molecular dynamics simulation of the frequency spectrum of amorphous silica. *J. Chem. Phys.* **1982**, *76*, 3189–3192.

(38) Henkelman, G.; Arnaldsson, A.; Jónsson, H. A fast and robust algorithm for Bader decomposition of charge density. *Comput. Mater Sci.* **2006**, *36*, 354–360.

(39) Sanville, E.; Kenny, S. D.; Smith, R.; Henkelman, G. Improved grid-based algorithm for Bader charge allocation. *J. Comput. Chem.* **2007**, *28*, 899–908.

(40) Tang, W.; Sanville, E.; Henkelman, G. A grid-based Bader analysis algorithm without lattice bias. *J. Phys. Condens. Matter* **2009**, *21*, 084204.

(41) Yu, M.; Trinkle, D. R. Accurate and efficient algorithm for Bader charge integration. *J. Chem. Phys.* **2011**, *134*, 064111.

(42) Birdja, Y. Y.; Pérez-Gallent, E.; Figueiredo, M. C.; Göttle, A. J.; Calle-Vallejo, F.; Koper, M. T. M. Advances and challenges in understanding the electrocatalytic conversion of carbon dioxide to fuels. *Nat. Energy* **2019**, *4*, 732–745.

(43) Tomboc, G. M.; Choi, S.; Kwon, T.; Hwang, Y. J.; Lee, K. Potential link between Cu surface and selective CO_2 electroreduction: Perspective on future electrocatalyst designs. *Adv. Mater.* **2020**, *32*, 1908398.

(44) Schedel-Niedrig, T.; Neisius, T.; Böttger, I.; Kitzelmann, E.; Weinberg, G.; Demuth, D.; Schlögl, R. Copper (sub)oxide formation: a surface sensitive characterization of model catalysts. *Phys. Chem. Chem. Phys.* **2000**, *2*, 2407–2417.

(45) Favaro, M.; Xiao, H.; Cheng, T.; Goddard, W. A.; Yano, J.; Crumlin, E. J. Subsurface oxide plays a critical role in CO_2 activation by Cu(111) surfaces to form chemisorbed CO_2, the first step in reduction of CO_2. *Proc. Natl. Acad. Sci. USA* **2017**, *114*, 6706–6711.

(46) Lee, S. Y.; Jung, H.; Kim, N.-K.; Oh, H.-S.; Min, B. K.; Hwang, Y. J. Mixed copper states in anodized Cu electrocatalyst for stable and selective ethylene production from CO_2 reduction. *J. Am. Chem. Soc.* **2018**, *140*, 8681–8689.

(47) Arán-Ais, R. M.; Scholten, F.; Kunze, S.; Rizo, R.; Roldan Cuenya, B. The role of in situ generated morphological motifs and Cu(I) species in C_{2+} product selectivity during CO_2 pulsed electroreduction. *Nat. Energy* **2020**, *5*, 317–325.

(48) Jung, H.; Lee, S. Y.; Lee, C. W.; Cho, M. K.; Won, D. H.; Kim, C.; Oh, H.-S.; Min, B. K.; Hwang, Y. J. Electrochemical fragmentation of Cu_2O nanoparticles enhancing selective C–C coupling from CO_2 reduction reaction. *J. Am. Chem. Soc.* **2019**, *141*, 4624–4633.

(49) Kim, D.; Lee, S.; Ocon, J. D.; Jeong, B.; Lee, J. K.; Lee, J. Insights into an autonomously formed oxygen-evacuated Cu_2O electrode for the selective production of C_2H_4 from CO_2. *Phys. Chem. Chem. Phys.* **2015**, *17*, 824–830.

(50) Lin, S.-C.; Chang, C.-C.; Chiu, S.-Y.; Pai, H.-T.; Liao, T.-Y.; Hsu, C.-S.; Chiang, W.-H.; Tsai, M.-K.; Chen, H. M. Operando time-resolved X-ray absorption spectroscopy reveals the chemical nature enabling highly selective CO_2 reduction. *Nat. Commun.* **2020**, *11*, 1–12.

(51) Eilert, A.; Cavalca, F.; Roberts, F. S.; Osterwalder, J.; Liu, C.; Favaro, M.; Crumlin, E. J.; Ogasawara, H.; Friebel, D.; Pettersson, L. G. M. et al. Subsurface oxygen in oxide-derived copper electrocatalysts for carbon dioxide reduction. *J. Phys. Chem. Lett.* **2017**, *8*, 285–290.

(52) Zhang, W.; Huang, C.; Xiao, Q.; Yu, L.; Shuai, L.; An, P.; Zhang, J.; Qiu, M.; Ren, Z.; Yu, Y. Atypical oxygen-bearing copper boosts ethylene selectivity toward electrocatalytic CO_2 reduction. *J. Am. Chem. Soc.* **2020**, *142*, 11417–11427.

(53) Möller, T.; Scholten, F.; Thanh, T. N.; Sinev, I.; Timoshenko, J.; Wang, X.; Jovanov, Z.; Gliech, M.; Cuenya, B. R.; Varela, A. S. et al. Electrocatalytic CO_2 reduction on CuO_x nanocubes tracking the evolution of chemical state, geometric structure,

and catalytic selectivity using Operando Spectroscopy. *Angew. Chem. Int. Ed.* **2020**, DOI: 10.1002/anie.202007136.

(54) Bai, H.; Cheng, T.; Li, S.; Zhou, Z.; Yang, H.; Li, J.; Xie, M.; Ye, J.; Ji, Y.; Li, Y. et al. Controllable CO adsorption determines ethylene and methane productions from CO_2 electroreduction. *Sci. Bull.* **2020**, DOI: 10.1016/j.scib.2020.06.023.

(55) Lee, S.; Kim, D.; Lee, J. Electrocatalytic production of C3-C4 compounds by conversion of CO_2 on a chloride-induced bi-phasic Cu_2O-Cu catalyst. *Angew. Chem. Int. Ed.* **2015**, *54*, 14701–14705.

(56) Mistry, H.; Varela, A. S.; Bonifacio, C. S.; Zegkinoglou, I.; Sinev, I.; Choi, Y.-W.; Kisslinger, K.; Stach, E. A.; Yang, J. C.; Strasser, P. et al. Highly selective plasma-activated copper catalysts for carbon dioxide reduction to ethylene. *Nat. Commun.* **2016**, 12123.

(57) De Luna, P.; Quintero-Bermudez, R.; Dinh, C.-T.; Ross, M. B.; Bushuyev, O. S.; Todorović, P.; Regier, T.; Kelley, S. O.; Yang, P.; Sargent, E. H. Catalyst electro-redeposition controls morphology and oxidation state for selective carbon dioxide reduction. *Nat. Catal.* **2018**, *1*, 103–110.

(58) Yang, P.-P.; Zhang, X.-L.; Gao, F.-Y.; Zheng, Y.-R.; Niu, Z.-Z.; Yu, X.; Liu, R.; Wu, Z.-Z.; Qin, S.; Chi, L.-P. et al. Protecting copper oxidation state via intermediate confinement for selective CO_2 electroreduction to C_{2+} fuels. *J. Am. Chem. Soc.* **2020**, *142*, 6400–6408.

(59) Lum, Y.; Ager, J. W. Evidence for product-specific active sites on oxide-derived Cu catalysts for electrochemical CO_2 reduction. *Nat. Catal.* **2019**, *2*, 86–93.

(60) He, M.; Li, C.; Zhang, H.; Chang, X.; Chen, J. G.; Goddard III, W. A.; Cheng, M.-j.; Xu, B.; Lu, Q. Oxygen induced promotion of electrochemical reduction of CO_2 via co-electrolysis. *Nat. Commun.* **2020**, *11*, 3844.

(61) Kim, Y. G.; Soriaga, M. P. Cathodic regeneration of a clean and ordered Cu(100)-(1×1) surface from an air-oxidized and disordered electrode: An operando STM study. *J. Electroanal. Chem.* **2014**, *734*, 7–9.

(62) Scott, S. B.; Hogg, T. V.; Landers, A. T.; Maagaard, T.; Bertheussen, E.; Lin, J. C.; Davis, R. C.; Beeman, J. W.; Higgins, D.; Drisdell, W. S. et al. Absence of oxidized phases in Cu under CO reduction conditions. *ACS Energy Lett.* **2019**, *4*, 803–804.

(63) Velasco-Velez, J.-J.; Mom, R. V.; Sandoval-Diaz, L.-E.; Falling, L. J.; Chuang, C.-h.; Gao, D.; Jones, T. E.; Zhu, Q.; Arrigo, R.; Cuenya, B. R. et al. Revealing the active phase of copper during the electroreduction of CO_2 in aqueous electrolyte by correlating *In Situ* X-ray spectroscopy and *In Situ* electron microscopy. *ACS Energy Lett.* **2020**, *5*, 2106–2111.

(64) Lum, Y.; Ager, J. W. Stability of residual oxides in oxide-derived copper catalysts for electrochemical CO_2 reduction investigated with ^{18}O labeling. *Angew. Chem. Int. Ed.* **2018**, *57*, 551–554.

(65) Khanipour, P.; Löffler, M.; Reichert, A. M.; Haase, F. T.; Mayrhofer, K. J. J.; Katsounaros, I. Electrochemical Real-Time Mass Spectrometry (EC-RTMS): Monitoring electrochemical reaction products in real time. *Angew. Chem. Int. Ed.* **2019**, *58*.

(66) Handoko, A. D.; Wei, F.; Jenndy,; Yeo, B. S.; Seh, Z. W. Understanding heterogeneous electrocatalytic carbon dioxide reduction through operando techniques. *Nat. Catal.* **2018**, *1*, 922–934.

(67) Mandal, L.; Yang, K. R.; Motapothula, M. R.; Ren, D.; Lobaccaro, P.; Patra, A.; Sherburne, M.; Batista, V. S.; Yeo, B. S.; Ager, J. W. et al. Investigating the role of copper oxide in electrochemical CO_2 reduction in real time. *ACS Appl. Mater. Interfaces* **2018**, *10*, 8574–8584.

(68) Ren, D.; Deng, Y.; Handoko, A. D.; Chen, C. S.; Malkhandi, S.; Yeo, B. S. Selective electrochemical reduction of carbon dioxide to ethylene and ethanol on copper(I) oxide catalysts. *ACS Catal.* **2015**, *5*, 2814–2821.

(69) Hori, Y.; Takahashi, I.; Koga, O.; Hoshi, N. Electrochemical reduction of carbon dioxide at various series of copper single crystal electrodes. *J. Mol. Catal. Chem.* **2003**, *199*, 39–47.

(70) Bagger, A.; Ju, W.; Varela, A. S.; Strasser, P.; Rossmeisl, J. Electrochemical CO_2 reduction: Classifying Cu facets. *ACS Catal.* **2019**, *9*, 7894–7899.

(71) Kim, Y. G.; Baricuatro, J. H.; Javier, A.; Gregoire, J. M.; Soriaga, M. P. The evolution of the polycrystalline copper surface, first to Cu(111) and then to Cu(100), at a fixed CO_2RR potential: A study by operando EC-STM. *Langmuir* **2014**, *30*, 15053–15056.

(72) Huang, J.; Hörmann, N.; Oveisi, E.; Loiudice, A.; De Gregorio, G. L.; Andreussi, O.; Marzari, N.; Buonsanti, R. Potential-induced nanoclustering of metallic catalysts during electrochemical CO_2 reduction. *Nat. Commun.* **2018**, *9*, 3117.

(73) Gao, D.; Arán-Ais, R. M.; Jeon, H. S.; Roldan-Cuenya, B. Rational catalyst and electrolyte design for CO_2 electroreduction towards multicarbon products. *Nat. Catal.* **2019**, *2*, 198–210.

(74) Liu, C.; Lourenço, M. P.; Hedström, S.; Cavalca, F.; Diaz-Morales, O.; Duarte, H. A.; Nilsson, A.; Pettersson, L. G. Stability and effects of subsurface oxygen in oxide-derived Cu catalyst for CO_2 reduction. *J. Phys. Chem. C* **2017**, *121*, 25010–25017.

(75) Fields, M.; Hong, X.; Nørskov, J. K.; Chan, K. Role of subsurface oxygen on Cu surfaces for CO_2 electrochemical reduction. *J. Phys. Chem. C* **2018**, *122*, 16209–16215.

(76) Garza, A. J.; Bell, A. T.; Head-Gordon, M. Is subsurface oxygen necessary for the electrochemical reduction of CO_2 on copper? *J. Phys. Chem. Lett.* **2018**, *9*, 601–606.

(77) Ma, M.; Djanashvili, K.; Smith, W. A. Controllable hydrocarbon formation from the electrochemical reduction of CO_2 over Cu nanowire arrays. *Angew. Chem. Int. Ed.* **2016**, *55*, 6680–6684.

(78) Wang, Y.; Wang, Z.; Dinh, C.-T.; Li, J.; Ozden, A.; Kibria, M. G.; Seifitokaldani, A.; Tan, C.-S.; Gabardo, C. M.; Luo, M. et al. Catalyst synthesis under CO_2 electroreduction favours faceting and promotes renewable fuels electrosynthesis. *Nat. Catal.* **2019**, *3*, 98–106.

(79) Liu, C.; Hedström, S.; Stenlid, J. H.; Pettersson, L. G. Amorphous, periodic model of a copper electrocatalyst with subsurface oxygen for enhanced CO coverage and dimerization. *J. Phys. Chem. C* **2019**, *123*, 4961–4968.

(80) Ringe, S.; Morales-Guio, C. G.; Chen, L. D.; Fields, M.; Jaramillo, T. F.; Hahn, C.; Chan, K. Double layer charging driven carbon dioxide adsorption limits the rate of electrochemical carbon dioxide reduction on Gold. *Nat. Commun.* **2020**, *11*, 33.

(81) Veenstra, F. L.; Ackerl, N.; Martín, A. J.; Pérez-Ramírez, J. Laser-microstructured copper reveals selectivity patterns in the electrocatalytic reduction of CO_2. *Chem* **2020**, *6*, 1707–1722.

(82) Bohra, D.; Chaudhry, J. H.; Burdyny, T.; Pidko, E. A.; Smith, W. A. Modeling the electrical double layer to understand the reaction environment in a CO_2 electrocatalytic system. *Energy Environ. Sci.* **2019**, *12*, 3380–3389.

(83) Zhang, F.; Co, A. C. Direct evidence of local pH change and the role of alkali cation during CO_2 electroreduction in aqueous media. *Angew. Chem. Int. Ed.* **2020**, *59*, 1674–1681.

(84) Li, C. W.; Ciston, J.; Kanan, M. W. Electroreduction of carbon monoxide to liquid fuel on oxide-derived nanocrystalline copper. *Nature* **2014**, *508*, 504–507.

(85) Yang, F.; Choi, Y.; Liu, P.; Hrbek, J.; Rodriguez, J. A. Autocatalytic reduction of a Cu_2O/Cu(111) surface by CO: STM, XPS, and DFT studies. *J. Phys. Chem. C* **2010**, *114*, 17042–17050.

(86) Deng, Y.; Handoko, A. D.; Du, Y.; Xi, S.; Yeo, B. S. In Situ Raman spectroscopy of copper and copper oxide surfaces during electrochemical oxygen evolution reaction: Identification of Cu^{III} oxides as catalytically active species. *ACS Catal.* **2016**, *6*, 2473–2481.

(87) Zhao, Y.; Chang, X.; Malkani, A. S.; Yang, X.; Thompson, L.; Jiao, F.; Xu, B. Speciation of Cu surfaces during the electrochemical CO reduction reaction. *J. Am. Chem. Soc.* **2020**, *142*, 9735–9743.

(88) Jeong, H. M.; Kwon, Y.; Won, J. H.; Lum, Y.; Cheng, M.-j.; Kim, K. H.; Head-gordon, M.; Kang, J. K. Atomic-scale spacing between copper facets for the electrochemical reduction of carbon dioxide. *Adv. Energy Mater.* **2020**, *10*.

(89) Gao, J.; Ren, D.; Guo, X.; Zakeeruddin, S. M.; Grätzel, M. Sequential catalysis enables enhanced C–C coupling towards multi-carbon alkenes and alcohols in carbon dioxide reduction: a study on bifunctional Cu/Au electrocatalysts. *Faraday Discuss.* **2019**, *215*, 282–296.

(90) Liang, Z.-Q.; Zhuang, T.-T.; Seifitokaldani, A.; Li, J.; Huang, C.-W.; Tan, C.-S.; Li, Y.; De Luna, P.; Dinh, C. T.; Hu, Y. et al. Copper-on-nitride enhances the stable electrosynthesis of multi-carbon products from CO_2. *Nat. Commun.* **2018**, *9*, 3828.

(91) Verdaguer-Casadevall, A.; Li, C. W.; Johansson, T. P.; Scott, S. B.; McKeown, J. T.; Kumar, M.; Stephens, I. E.; Kanan, M. W.; Chorkendorff, I. Probing the active surface

sites for CO reduction on oxide-derived copper electrocatalysts. *J. Am. Chem. Soc.* **2015**, *137*, 9808–9811.

(92) Zhuang, T.-T.; Liang, Z.-Q.; Seifitokaldani, A.; Li, Y.; De Luna, P.; Burdyny, T.; Che, F.; Meng, F.; Min, Y.; Quintero-Bermudez, R. et al. Steering post-C–C coupling selectivity enables high efficiency electroreduction of carbon dioxide to multi-carbon alcohols. *Nat. Catal.* **2018**, *1*, 421–428.

(93) Gao, D.; McCrum, I. T.; Deo, S.; Choi, Y.-W.; Scholten, F.; Wan, W.; Chen, J. G.; Janik, M. J.; Roldan Cuenya, B. Activity and selectivity control in CO_2 electroreduction to multicarbon products over CuO_x catalysts via electrolyte design. *ACS Catal.* **2018**, *8*, 10012–10020.

(94) Zhou, Y.; Che, F.; Liu, M.; Zou, C.; Liang, Z.; De Luna, P.; Yuan, H.; Li, J.; Wang, Z.; Xie, H. et al. Dopant-induced electron localization drives CO_2 reduction to C_2 hydrocarbons. *Nat. Chem.* **2018**, *10*, 974–980.

(95) Li, J.; Wang, Z.; McCallum, C.; Xu, Y.; Li, F.; Wang, Y.; Gabardo, C. M.; Dinh, C.-T.; Zhuang, T.-T.; Wang, L. et al. Constraining CO coverage on copper promotes high-efficiency ethylene electroproduction. *Nat. Catal.* **2019**, *2*, 1124–1131.

(96) Li, F.; Thevenon, A.; Rosas-Hernández, A.; Wang, Z.; Li, Y.; Gabardo, C. M.; Adnan, O.; Cao, T. D.; Li, J.; Wang, Y. et al. Molecular tuning of CO_2-to-ethylene conversion. *Nature* **2019**, *577*, 509–513.

(97) Dinh, C.-T.; Burdyny, T.; Kibria, M. G.; Seifitokaldani, A.; Gabardo, C. M.; García de Arquer, F. P.; Kiani, A.; Edwards, J. P.; De Luna, P.; Bushuyev, O. S. et al. CO_2 electroreduction to ethylene via hydroxide-mediated copper catalysis at an abrupt interface. *Science* **2018**, *360*, 783–787.

(98) Gao, Y.; Wu, Q.; Liang, X.; Wang, Z.; Zheng, Z.; Wang, P.; Liu, Y.; Dai, Y.; Whangbo, M.-H.; Huang, B. Cu_2O nanoparticles with both {100} and {111} facets

for enhancing the selectivity and activity of CO_2 electroreduction to ethylene. *Adv. Sci.* **2020**, *7*, 1902820.

(99) Kim, T.; Palmore, G. T. R. A scalable method for preparing Cu electrocatalysts that convert CO_2 into C_{2+} products. *Nat. Commun.* **2020**, *11*, 3622.

(100) Shang, L.; Lv, X.; Shen, H.; Shao, Z.; Zheng, G. Selective carbon dioxide electroreduction to ethylene and ethanol by core-shell copper/cuprous oxide. *J. Colloid. Interface Sci.* **2019**, *552*, 426–431.

(101) Kibria, M. G.; Dinh, C.-T.; Seifitokaldani, A.; De Luna, P.; Burdyny, T.; Quintero-Bermudez, R.; Ross, M. B.; Bushuyev, O. S.; García de Arquer, F. P.; Yang, P. et al. A surface reconstruction route to high productivity and selectivity in CO_2 electroreduction toward C_{2+} hydrocarbons. *Adv. Mater.* **2018**, *30*, 1804867.

(102) Wu, D.; Dong, C.; Wu, D.; Fu, J.; Liu, H.; Hu, S.; Jiang, Z.; Qiao, S. Z.; Du, X. W. Cuprous ions embedded in ceria lattice for selective and stable electrochemical reduction of carbon dioxide to ethylene. *J. Mater. Chem. A* **2018**, *6*, 9373–9377.

(103) Nam, D.-H.; Bushuyev, O. S.; Li, J.; De Luna, P.; Seifitokaldani, A.; Dinh, C.-T.; García de Arquer, F. P.; Wang, Y.; Liang, Z.; Proppe, A. H. et al. Metal–organic frameworks mediate Cu coordination for selective CO_2 electroreduction. *J. Am. Chem. Soc.* **2018**, *140*, 11378–11386.

(104) Handoko, A. D.; Ong, C. W.; Huang, Y.; Lee, Z. G.; Lin, L.; Panetti, G. B.; Yeo, B. S. Mechanistic insights into the selective electroreduction of carbon dioxide to ethylene on Cu_2O-derived copper catalysts. *J. Phys. Chem. C* **2016**, *120*, 20058–20067.

(105) Loiudice, A.; Lobaccaro, P.; Kamali, E. A.; Thao, T.; Huang, B. H.; Ager, J. W.; Buonsanti, R. Tailoring copper nanocrystals towards C_2 products in electrochemical CO_2 reduction. *Angew. Chem. Int. Ed.* **2016**, *55*, 5789–5792.

(106) Chou, T.-C.; Chang, C.-C.; Yu, H.-L.; Yu, W.-Y.; Dong, C.-L.; Velasco-Vélez, J.-J.; Chuang, C.-H.; Chen, L.-C.; Lee, J.-F.; Chen, J.-M. et al. Controlling the oxidation state of Cu electrode and reaction intermediates for electrochemical CO_2 reduction to ethylene. *J. Am. Chem. Soc.* **2020**, *142*, 2857–2867.

(107) Yang, K. D.; Ko, W. R.; Lee, J. H.; Kim, S. J.; Lee, H.; Lee, M. H.; Nam, K. T. Morphology-directed selective production of ethylene or ethane from CO_2 on a Cu mesopore electrode. *Angew. Chem. Int. Ed.* **2017**, *56*, 796–800.

(108) Altaf, N.; Liang, S.; Huang, L.; Wang, Q. Electro-derived Cu-Cu_2O nanocluster from LDH for stable and selective C_2 hydrocarbons production from CO_2 electrochemical reduction. *J. Energy Chem.* **2020**, *48*, 169–180.

(109) Huang, Y.; Handoko, A. D.; Hirunsit, P.; Yeo, B. S. Electrochemical reduction of CO_2 using copper single-crystal surfaces: Effects of CO* coverage on the selective formation of ethylene. *ACS Catal.* **2017**, *7*, 1749–1756.

(110) Jeon, H. S.; Kunze, S.; Scholten, F.; Roldan Cuenya, B. Prism-shaped Cu nanocatalysts for electrochemical CO_2 reduction to ethylene. *ACS Catal.* **2018**, *8*, 531–535.

(111) Dutta, A.; Rahaman, M.; Luedi, N. C.; Mohos, M.; Broekmann, P. Morphology matters: tuning the product distribution of CO_2 electroreduction on oxide-derived Cu foam catalysts. *ACS Catal.* **2016**, *6*, 3804–3814.

(112) Reske, R.; Mistry, H.; Behafarid, F.; Roldan Cuenya, B.; Strasser, P. Particle size effects in the catalytic electroreduction of CO_2 on Cu nanoparticles. *J. Am. Chem. Soc.* **2014**, *136*, 6978–6986.

(113) Ting, L. R. L.; Piqué, O.; Lim, S. Y.; Tanhaei, M.; Calle-Vallejo, F.; Yeo, B. S. Enhancing CO_2 electroreduction to ethanol on copper-silver composites by opening an alternative catalytic pathway. *ACS Catal.* **2020**, *10*, 4059–4069.

(114) Xu, H.; Rebollar, D.; He, H.; Chong, L.; Liu, Y.; Liu, C.; Sun, C.-j.; Li, T.; Muntean, J. V.; Winans, R. E. et al. Highly selective electrocatalytic CO_2 reduction to ethanol by metallic clusters dynamically formed from atomically dispersed copper. *Nat. Energy* **2020**, *5*, 623–632.

(115) Wang, L.; Nitopi, S.; Wong, A. B.; Snider, J. L.; Nielander, A. C.; Morales-Guio, C. G.; Orazov, M.; Higgins, D. C.; Hahn, C.; Jaramillo, T. F. Electrochemically converting carbon monoxide to liquid fuels by directing selectivity with electrode surface area. *Nat. Catal.* **2019**, *2*, 702–708.

(116) Wang, X.; Wang, Z.; García de Arquer, F. P.; Dinh, C.-T.; Ozden, A.; Li, Y. C.; Nam, D.-H.; Li, J.; Liu, Y.-S.; Wicks, J. et al. Efficient electrically powered CO_2-to-ethanol via suppression of deoxygenation. *Nat. Energy* **2020**, *5*, 478–486.

(117) Li, Y. C.; Wang, Z.; Yuan, T.; Nam, D.-H.; Luo, M.; Wicks, J.; Chen, B.; Li, J.; Li, F.; García de Arquer, F. P. et al. Binding site diversity promotes CO_2 electroreduction to ethanol. *J. Am. Chem. Soc.* **2019**, *141*, 8584–8591.

(118) Li, F.; Li, Y. C.; Wang, Z.; Li, J.; Nam, D.-H.; Lum, Y.; Luo, M.; Wang, X.; Ozden, A.; Hung, S.-F. et al. Cooperative CO_2-to-ethanol conversion via enriched intermediates at molecule–metal catalyst interfaces. *Nat. Catal.* **2020**, *3*, 75–82.

(119) Lee, S.; Park, G.; Lee, J. Importance of Ag–Cu biphasic boundaries for selective electrochemical reduction of CO_2 to ethanol. *ACS Catal.* **2017**, *7*, 8594–8604.

(120) Wang, H.; Tzeng, Y.-K.; Ji, Y.; Li, Y.; Li, J.; Zheng, X.; Yang, A.; Liu, Y.; Gong, Y.; Cai, L. et al. Synergistic enhancement of electrocatalytic CO_2 reduction to C_2 oxygenates at nitrogen-doped nanodiamonds/Cu interface. *Nat. Nanotechnol.* **2020**, *15*, 131–137.

(121) Wang, X.; Wang, Z.; Zhuang, T.-T.; Dinh, C.-T.; Li, J.; Nam, D.-H.; Li, F.; Huang, C.-

W.; Tan, C.-S.; Chen, Z. et al. Efficient upgrading of CO to C_3 fuel using asymmetric C–C coupling active sites. *Nat. Commun.* **2019**, *10*, 5186.

(122) Li, J.; Che, F.; Pang, Y.; Zou, C.; Howe, J. Y.; Burdyny, T.; Edwards, J. P.; Wang, Y.; Li, F.; Wang, Z. et al. Copper adparticle enabled selective electrosynthesis of *n*-propanol. *Nat. Commun.* **2018**, *9*, 4614.

(123) Pang, Y.; Li, J.; Wang, Z.; Tan, C.-S.; Hsieh, P.-L.; Zhuang, T.-T.; Liang, Z.-Q.; Zou, C.; Wang, X.; De Luna, P. et al. Efficient electrocatalytic conversion of carbon monoxide to propanol using fragmented copper. *Nat. Catal.* **2019**, *2*, 251–258.

(124) Ren, D.; Wong, N. T.; Handoko, A. D.; Huang, Y.; Yeo, B. S. Mechanistic insights into the enhanced activity and stability of agglomerated Cu nanocrystals for the electrochemical reduction of carbon dioxide to *n*-Propanol. *J. Phys. Chem. Lett.* **2016**, *7*, 20–24.

(125) Rudd, J. A.; Kazimierska, E.; Hamdy, L. B.; Bain, O. J. E.; Ahn, S.; Barron, A. R.; Andreoli, E. CO_2 reduction to propanol by copper foams: A pre- and post-catalysis study. **2020**, doi: 10.26434/chemrxiv.12022623.v1.

(126) Mistry, H.; Choi, Y.-W.; Bagger, A.; Scholten, F.; Bonifacio, C. S.; Sinev, I.; Divins, N. J.; Zegkinoglou, I.; Jeon, H. S.; Kisslinger, K. et al. Enhanced carbon dioxide electroreduction to carbon monoxide over defect-rich plasma-activated silver catalysts. *Angew. Chem. Int. Ed.* **2017**, *56*, 11394–11398.

(127) Ni, W.; Li, C.; Zang, X.; Xu, M.; Huo, S.; Liu, M.; Yang, Z.; Yan, Y.-M. Efficient electrocatalytic reduction of CO_2 on Cu_xO decorated graphene oxides: An insight into the role of multivalent Cu in selectivity and durability. *Appl. Catal.* **2019**, *259*, 118044.

(128) Yu, J.; Namba, Y. Atomic surface roughness. *Appl. Phys. Lett.* **1998**, *73*, 3607–3609.

(129) Heyes, J.; Dunwell, M.; Xu, B. CO_2 reduction on Cu at low overpotentials with surface-enhanced in situ spectroscopy. *J. Phys. Chem. C* **2016**, *120*, 17334–17341.

(130) Pérez-Gallent, E.; Figueiredo, M. C.; Calle-Vallejo, F.; Koper, M. T. M. Spectroscopic observation of a hydrogenated CO dimer intermediate during CO reduction on Cu(100) electrodes. *Angew. Chem. Int. Ed.* **2017**, *56*, 3621–3624.

(131) Lee, S. H.; Sullivan, I.; Larson, D. M.; Liu, G.; Toma, F. M.; Xiang, C.; Drisdell, W. S. Correlating oxidation state and surface area to activity from *Operando* studies of copper CO electroreduction catalysts in a gas-fed device. *ACS Catal.* **2020**, *10*, 8000–8011.

(132) García-Muelas, R.; Dattila, F.; Shinagawa, T.; Martín, A. J.; Pérez-Ramírez, J.; López, N. Origin of the selective electroreduction of carbon dioxide to formate by chalcogen modified copper. *J. Phys. Chem. Lett.* **2018**, *9*, 7153–7159.

(133) Hori, Y.; Koga, O.; Yamazaki, H.; Matsuo, T. Infrared spectroscopy of adsorbed CO and intermediate species in electrochemical reduction of CO_2 to hydrocarbons on a Cu electrode. *Electrochim. Acta* **1995**, *40*, 2617–2622.

(134) Zhu, S.; Jiang, B.; Cai, W.-B.; Shao, M. Direct observation on reaction intermediates and the role of bicarbonate anions in CO_2 electrochemical reduction reaction on Cu surfaces. *J. Am. Chem. Soc.* **2017**, *139*, 15664–15667.

(135) Łukomska, A.; Sobkowski, J. Potential of zero charge of monocrystalline copper electrodes in perchlorate solutions. *J. Electroanal. Chem.* **2004**, *567*, 95–102.